The effect of track load correlation on ground-borne vibration from railways

Evangelos Ntotsios [a*], David Thompson [a], Mohammed Hussein [b]

[a] *Institute of Sound and Vibration Research, University of Southampton, Southampton SO17 1BJ, UK*
[b] *Department of Civil and Architectural Engineering, Qatar University, Doha, 2713, Qatar*

Abstract

In predictions of ground-borne vibration from railways, it is generally assumed that the unevenness profile of the wheel and rail is fully correlated between the two rails and the two wheels of an axle. This leads to identical contact forces at the two rails and can allow further simplifications of the vehicle model, the track model and the track/ground interface conditions. In the present paper, the level of correlation of the track loading at the wheel/rail interface due to rail unevenness and its influence on predictions of ground vibration is investigated. The extent to which the unevenness of the two rails is correlated has been estimated from measurements of track geometry obtained with track recording vehicles for four different tracks. It was found that for wavelengths longer than about 3 m the unevenness of the two rails can be considered to be strongly correlated and in phase. To investigate the effect of this on ground vibration, an existing model expressed in the wavenumber-frequency domain is extended to include separate inputs on the two rails. The track is modelled as an infinite invariant linear structure resting on an elastic stratified half-space. This is excited by the gravitational loading of a passing train and the irregularity of the contact surfaces between the wheels and the rails. The railway model is developed in this work to be versatile so that it can account or discard the effect of load correlations on the two rails beside the effects of variation of the tractions across the width of the track-ground interface and the vehicle sprung mass, as well as the roll motion of the sleepers and the axle. A comparative analysis is carried out on the influence of these factors on the response predictions using numerical simulations. It is shown that, when determining the vibration in the free field, it is important to include in the model the traction variation across the track-ground interface and the non-symmetrical loading at the two rails that occurs for unevenness wavelengths shorter than about 3 m.

Key Words: Ground-borne vibration, track unevenness correlation, wavenumber-frequency domain model.

[*]Corresponding author, *Email address*: E.Ntotsios@soton.ac.uk
Email address: djt@isvr.soton.ac.uk (David Thompson), mhussein@qu.edu.qa (Mohammed Hussein).

1. Introduction

An important environmental impact of existing and future railway lines occurs due to the ground-borne vibration induced by the trains; this is an issue both for trains running on surface railways and for trains in tunnels. Ground-borne vibration from railways is generated at the wheel-rail interface due to the passage of individual wheel loads along the track (quasi-static loading) and due to dynamic interaction forces caused by irregularities of the wheels and tracks (dynamic loading) [1]. The vibration generated propagates through the ground to nearby buildings where it may cause annoyance to people or malfunctioning of sensitive equipment. Inhabitants of the buildings perceive the vibration either directly, due to motion of floors and walls, or indirectly as re-radiated noise.

Modelling ground-borne vibration from railways is essential for understanding the physics of its generation and propagation. A good understanding is important in identifying ways to tackle unacceptable levels of vibration from existing as well as future railway lines. Many different numerical models have been developed for predicting vibration from surface and underground railways in the last few decades. A comprehensive overview of the state of the art on railway-induced ground vibration models and the underlying excitation mechanisms can be found in [2].

The models for predicting ground-borne vibration are commonly developed by coupling sub-models for the train, the track and the ground and all are based to some extent upon simplifying assumptions. These may depend on engineering insight to replicate the operational conditions of interest, or may be necessary due to a lack of complete data for the simulation, or limitations in the available computational power. Although essential for the realization of the modelling effort, these simplifying assumptions introduce inaccuracies and uncertainties into the predictions, which in many cases remain unquantified.

Since neither the wheel nor the rail running surfaces are entirely smooth, their unevenness causes the wheel and rail to move vertically relative to one another. Thus, dynamic forces are generated at the wheel/rail contacts by the combined irregular profile of the rail and wheel running surfaces and these forces can lead to wave propagation in the ground. For the frequency range 2-80 Hz, typically of interest for the perception of ground vibration and 20-250 Hz for the perception of ground-borne noise, and a train speed range of 10-100 m/s (36-360 km/h), the corresponding wavelengths of the vertical unevenness lie within the range 0.04 to 50 m (or wavenumbers from 0.12 to 160 rad/m). When considering the rail surface, at wavelengths less than about 1 m this vertical unevenness is most commonly caused by irregular wear or corrugation of the rail contact surface, whereas at much longer wavelengths it is due to undulations in the track bed. On the wheels, short wavelength unevenness is again caused by wear whereas discrete wavelengths up to about 3 m are present due to out-of-roundness. Additionally, dynamic forces are generated as impacts as the wheels traverse switches and crossings or badly maintained rail joints [3-4].

A simplifying practice commonly used in most models for ground-borne vibration is that the forces generated at the wheel-rail interface are assumed to be identical (and in phase) for the two rails [e.g. 5-11]. This assumption implies that the unevenness of the two rails is identical and thus may be treated as a fully correlated input on the two rails. This seems reasonable for wavelengths much longer than around 1.2 m, which is twice the typical sleeper or fastener spacing, as the unevenness in this range corresponds to the track geometry. Consequently, this assumption can allow further simplification of the track model by using a single beam to represent both rails and considering the wheelset as a single mass [5, 7, 10, 11]. However, at shorter wavelengths, as used in models that predict rolling noise, the excitation on each rail should be treated as independent and the overall response determined by assuming that the roughness on both rails is uncorrelated. Thus the mean-square responses, due to separate excitation on the two rails, should be added [1].

Measurements of track geometry that can include very long wavelengths are obtained from track recording coaches (TRC) and are principally used to determine the need for track maintenance such as tamping of the ballast [12]. These systems measure the longitudinal profile of both rails, usually under loaded conditions. The minimum wavelength measured is usually around 1 m. In contrast, hand-held accelerometer-based trolleys and mechanical displacement probes are used to measure shorter wavelength rail irregularities ("acoustic roughness") up to wavelengths of about 1 m in unloaded conditions [1]. These measure one rail at a time and therefore do not allow the correlation between the two rails to be determined. To cover the complete wavelength interval required, a combination of measurement methods is needed [13-14].

The aim of this work is to identify the degree of correlation between the unevenness of the two rails and how it affects the vibration prediction in the free field when it is taken into account in the modelling.

There is little information available about the correlation between the unevenness on two rails of a track or two wheels of a wheelset apart from a few examples in [15]. In Section 2, some track geometry measurements obtained with TRCs are therefore shown for different operational railway tracks and the level of correlation between the unevenness of the two rails is investigated for the wavelength range 0.5-25 m. Moreover, in order to investigate and quantify the effects on the response predictions of ground-borne vibration caused by the level of correlation between the two rails, a surface railway model is presented in Section 3 describing the dynamic system of a ballasted (or slab) track on a layered elastic half-space and taking into account the traction variation across the track-ground interface, similarly to the formulation in [16]. The rotation of the track and the wheelsets about the axial direction (roll) is included as well as the vertical motion, allowing the introduction of different unevenness on the two rails. In Section 4, the effect of treating the unevenness of the two rails as fully correlated, partially correlated or uncorrelated is illustrated by calculating and comparing the dynamic response predictions in the free-field for a range of model/excitation parameters.

It should be noted that, in the present work, the wheel irregularities are neglected, so that all irregularities are assumed to be on the rail surface. Nonetheless, it has been shown in [17] that although the typical wheel irregularities are of a similar order of magnitude to the rail irregularities at short wavelengths (below 0.1 m; "acoustic roughness"), the magnitude of wheel irregularities is very much smaller than those of the rail at longer wavelengths and thus can be neglected for ground-borne vibration generation. This smooth-wheel assumption is a useful starting point for a more realistic input excitation in comparing the effectiveness of various ground-borne vibration prediction models.

2. Unevenness correlation between the rails

To demonstrate the level of correlation between the unevenness of the two rails, example spectra of measured track geometry data are presented. The data has been obtained with track recording coaches (TRC) for four operational railway tracks. Details of these track sections are given in Table 1. The first is a typical mainline ballasted track [14], the second is a booted sleeper slab track section of a high speed line, the third is a typical suburban slab track in a tunnel and the fourth is a freight line. In each case, as is standard practice with track geometry recording, the data had been high-pass filtered to remove wavelengths longer than 35 m. The data were segmented into 1024-point segments (204.8 m long for the first two tracks, 256 m for the other two) and power spectra and cross spectra estimates were obtained using 50% overlap and applying a Hamming window on the segments.

Table 1. Details of the track sections for which measured data is presented.

Track	Length (km)	Sample spacing (m)	Segment length (m)
Mainline ballasted track	10	0.2	204.8
Booted sleeper high speed slab track	7.5	0.2	204.8
Suburban slab track	2.0	0.25	256
Freight line	3.3	0.25	256

Figure 1 shows the spectra of rail unevenness determined for both rails of each track section. These are expressed in one-third octave band form for ease of comparison. It can be seen that the rail unevenness level is similar for the two rails in each case while the high speed slab track in Figure 1(b) shows lower unevenness levels than the ballasted track for wavelengths longer than 1 m. For the suburban slab track in Figure 1(c) the unevenness level is similar to the mainline ballasted track for the wavelength range 5-13 m but higher outside this range. As might be expected, the freight track in Figure 1(d) seems to be in the poorest condition amongst the four tracks presented here, with levels of unevenness 10 dB higher in all one-third octave bands.

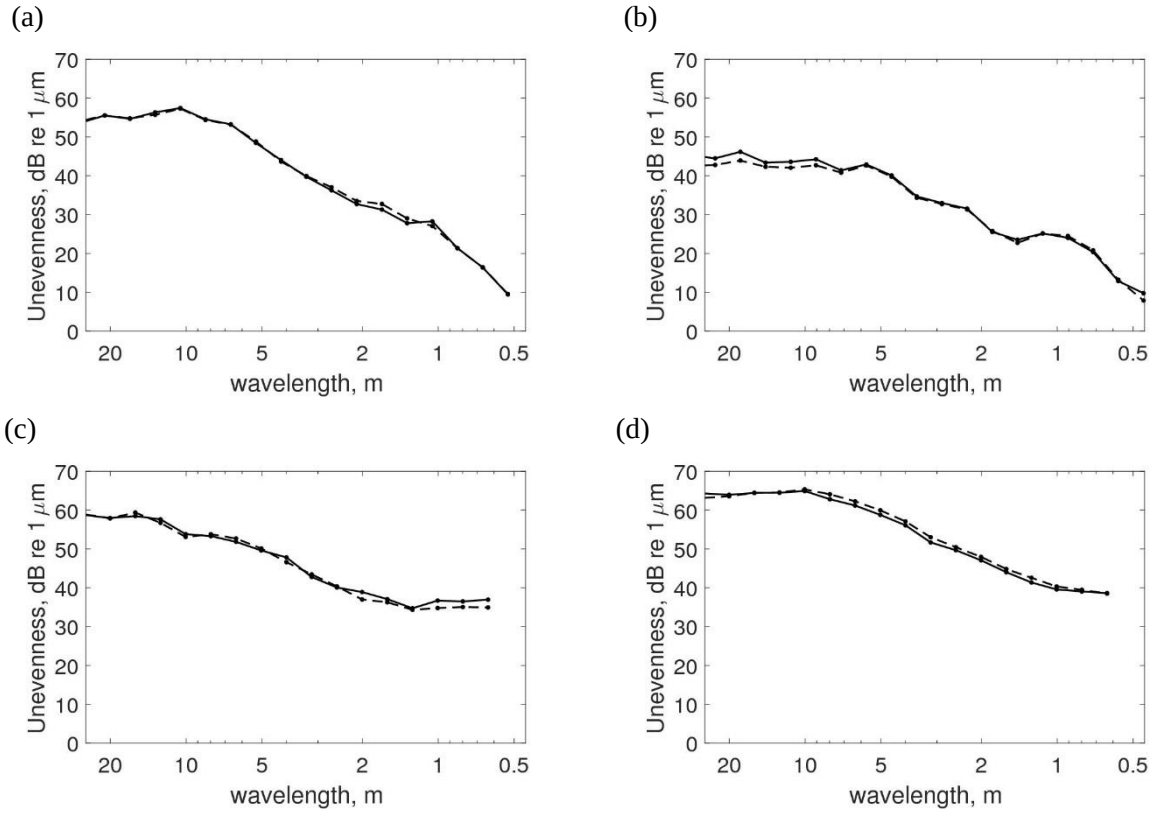

Figure 1. Measured unevenness spectrum in one third octave bands wavelength for (a) standard ballasted track [14], (b) high speed slab track, (c) standard slab track and (d) freight track:$(-)$ left and $(- - -)$ right rail.

Figure 2 shows the coherence function between the left and right rail profiles. The coherence function between two signals x and y is a real-valued function that is defined as

$$C_{xy}(\lambda) = \frac{\left|P_{xy}(\lambda)\right|^2}{P_{xx}(\lambda)P_{yy}(\lambda)} \tag{1}$$

where $P_{xy}(\lambda)$ is the cross-spectral density between x and y, and $P_{xx}(\lambda)$ and $P_{yy}(\lambda)$ the auto-spectral densities of x and y respectively. This provides a spectral quantification of the correlation between the unevenness of the two rails.

The coherence in Figure 2(a) and (b), for the ballasted track and the high speed slab track, is relatively high at long wavelengths, indicating that there is quite a strong correlation between the two rails. This occurs for wavelengths longer than about 3 m. A rise in the coherence can also be seen at a wavelength of about 0.6 m in each case which corresponds to the sleeper spacing due to the fact that the TRCs are measuring under loaded conditions. Similar results have been presented in [15]. The overall coherence for the suburban slab track in Figure 2(c) is much lower than for the other tracks and is high only at around 16 m, which is close to the typical length of rails historically used in the UK (18 m). For the case of the freight track in Figure 2(d) sharp peaks occur in the coherence function at certain

wavelengths (9 m, 6 m, 4.5 m 3.6 m etc.) which correspond to the existence of rail joints every 18 m, which is a typical distance for UK tracks.

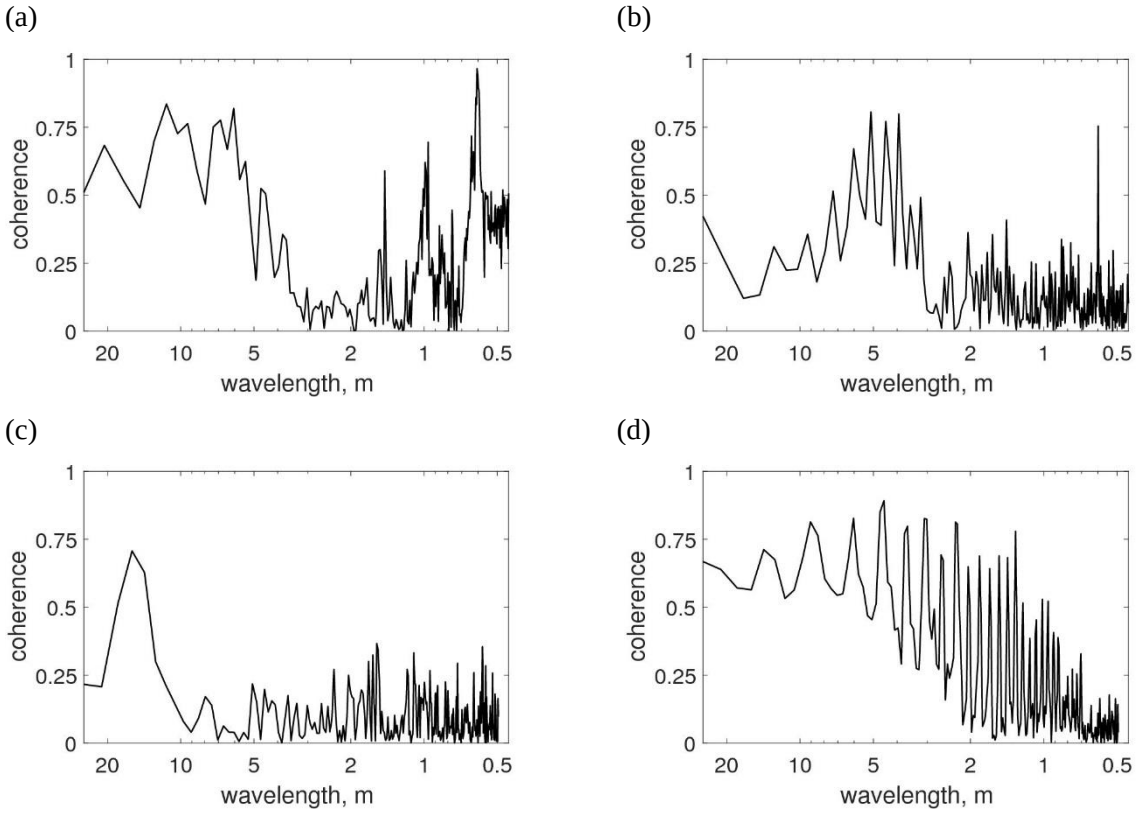

Figure 2. Coherence function for (a) standard ballasted track [14], (b) high speed slab track, (c) standard slab track and (d) freight track.

Figure 3 shows the relative phase between the left and right rail profiles, obtained from the phase of the cross-spectral density. This gives a reliable estimate of the relative phase only for wavelengths where the coherence is high. In each case, at wavelengths longer than about 3 m the unevenness of the two rails is in phase, apart from the suburban slab track for which the coherence is low.

In general, from Figures 2 and 3, it seems reasonable in most cases to assume that unevenness wavelengths longer than about 3 m can be treated as correlated or partially correlated between the two rails and in phase. These components of low frequency excitation are relevant to ground-borne vibration and are often important for feelable vibration. Nevertheless, discrete features such as wheel flats or rail joints are likely to be strongly correlated between the two rails even for quite short wavelengths. Nonetheless, apart from this, wavelengths shorter than about 3 m should be treated as uncorrelated between the two rails. For train speeds 36-360 km/h, irregularities shorter than 3 m correspond to excitation frequencies above 3-30 Hz which are well within the ground-borne vibration frequency range of interest. The influence on the ground vibration level of the degree of correlation between the

unevenness of the two rails will be investigated in Section 4 using simulated results. To achieve this a suitable model is first developed in the next section.

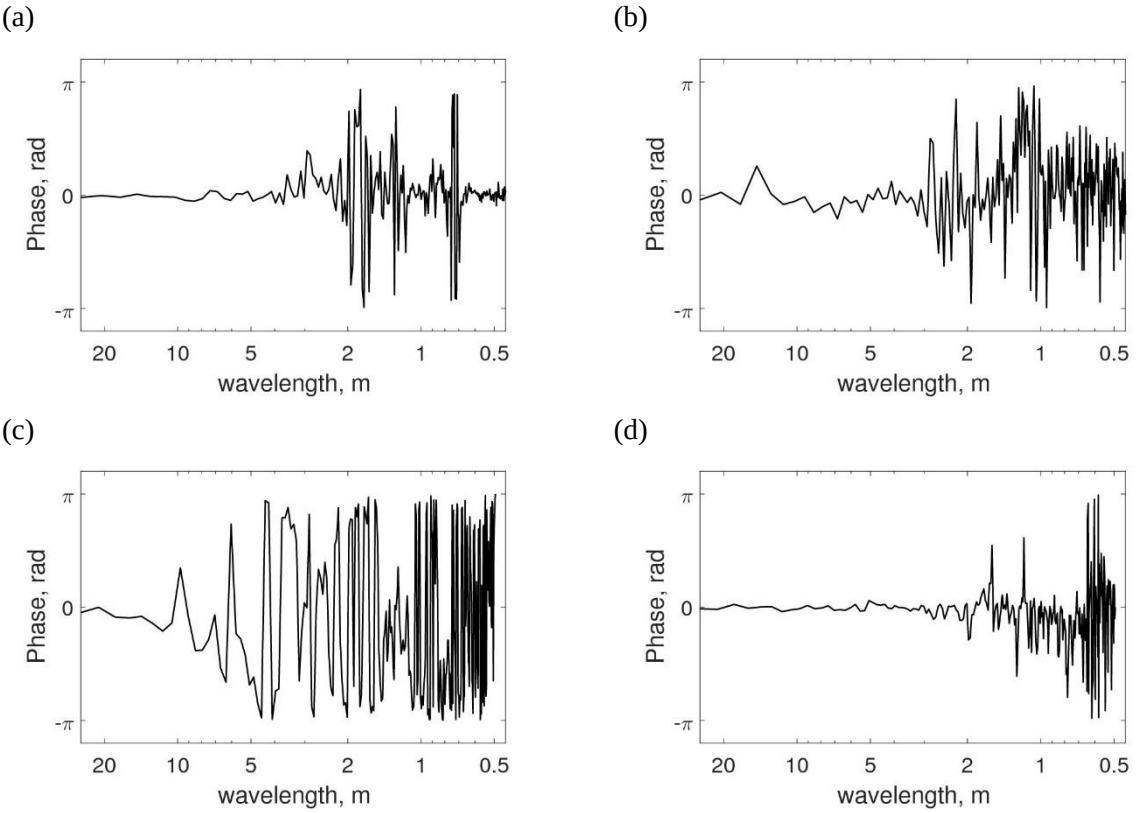

Figure 3. Relative phase between the rails unevenness for (a) standard ballasted track [14], (b) high speed slab track, (c) standard slab track and (d) freight track.

3. Wavenumber-frequency domain train-track-soil interaction model

To investigate the effects of correlation between the unevenness of the two rails, there is a need to consider the vehicle/track/soil interaction in more detail than is commonly used in the available frequency domain models. Accordingly, a model is presented here in which, as well as the vertical motion of the track and the wheelsets, their rotation about the axial direction is also taken into account by including both rails and both wheels of each axle separately. With this formulation, which is expressed in the wavenumber-frequency domain, different unevenness can be introduced on the two rails. The model is an extension of the one developed by Sheng et al. [5] and can include the effects of the moving loads and predict the vibration level at a fixed point in the free field.

3.1 General formulation for two rails in a moving frame

As in [5], the railway track considered in this paper is a straight ballasted or slab track at the surface of a layered elastic half-space, as shown in Figure 4(a). Linear dynamic behaviour is assumed throughout. The track is considered to be invariant in the longitudinal (x) direction and is modelled as multiple

beams supported by vertical springs with consistent mass. The model is formulated in the wavenumber-frequency domain where the vibration predictions are based on the transfer function matrices for the ground formulated in [5] in a frame of reference moving with each load with speed v. In the current work only the vertical dynamics are considered and thus scalar expressions of the vertical response due to vertical loading are presented. The model is extended here to take into account the traction variation across the track-ground interface while the track can include the excitation and response of both rails separately.

In the general case when both rails are included in the model, the indices s and p are used when referring to the left ($s, p = L$) or right ($s, p = R$) rail. The notation $H_{r,ps}(\hat{x}, \omega)$ is introduced for the response at a point $\hat{x} = x - a_l - vt$ of the p-th rail due to a unit harmonic load of angular frequency ω acting at $x = a_l + vt$ on the s-th rail. Similarly $H_{g,s}(\hat{x}, y, \omega)$ represents the response at a point $(\hat{x}, y)$ at the ground surface due to a unit harmonic load acting at $x = a_l + vt$ on the s-th rail. Then the displacement of the p-th rail (in the vertical direction and in the fixed frame of reference) due to a sequence of $2M$ loads of amplitude $\tilde{P}_{l,s}(\omega)$ with $l = 1,2, \ldots, M$ and $s = L, R$ is given by

$$w_{r,p}(x,t) = \sum_{l=1}^{M} \left[H_{r,pL}(\hat{x}, \omega) \tilde{P}_{l,L}(\omega) + H_{r,pR}(\hat{x}, \omega) \tilde{P}_{l,R}(\omega) \right] \mathrm{e}^{\mathrm{i}\omega t} \tag{2}$$

and the displacement of the ground surface as

$$w_g(x,y,t) = \sum_{l=1}^{M} \left[H_{g,L}(\hat{x}, y, \omega) \tilde{P}_{l,L}(\omega) + H_{g,R}(\hat{x}, y, \omega) \tilde{P}_{l,R}(\omega) \right] \mathrm{e}^{\mathrm{i}\omega t} \tag{3}$$

The transfer functions $H_{g,s}(\hat{x}, y, \omega)$, as functions of the moving Cartesian co-ordinates, are obtained through a two-dimensional inverse Fourier transform

$$H_{g,s}(\hat{x}, y, \omega) = \frac{1}{4\pi^2} \int_{-\infty}^{\infty} \int_{-\infty}^{\infty} \tilde{H}_{g,s}\left(k_x, k_y, \omega - k_x v\right) \mathrm{e}^{\mathrm{i}(k_x \hat{x} + k_y y)} \mathrm{d}k_x \mathrm{d}k_y \tag{4}$$

where $\tilde{H}_{g,s}\left(k_x, k_y, \omega - k_x v\right)$ is the solution for the ground response in the wavenumber domain (k_x, k_y) with respect to the coordinates $(\hat{x}, y)$ which is derived for a moving frame of reference. This may be implemented using a Fast Fourier transform (FFT), or through a standard quadrature. In the current work all calculations are achieved using the FFT. Similarly for the rails a one-dimensional Fourier transform is used:

$$H_{r,ps}(\hat{x}, \omega) = \frac{1}{2\pi} \int_{-\infty}^{\infty} \tilde{H}_{r,ps}(k_x, \omega - k_x v) \mathrm{e}^{\mathrm{i}k_x \hat{x}} \mathrm{d}k_x \tag{5}$$

These transfer functions are calculated for receiving frequencies $2\pi f = \omega - k_x v$ and denote the displacement for a fixed point (x,y) at the ground surface due to a unit moving load of angular frequency ω acting at $x = a_l$, where the relative motion between the position $x = a_l + vt$ of the l-th axle and the receiver gives rise to a Doppler shift.

Although the load is applied at a single non-zero frequency, or at zero frequency, the ground vibration is a transient signal with a broad frequency content. In order to calculate the spectrum of the response of the p-th rail S_{rp} or the ground S_g to the moving loads with a single angular frequency ω, Eqs (2) and (3) are Fourier transformed with respect to time [5]:

$$S_{r,p}(x, f; \omega) = \frac{1}{2\pi v} \mathrm{e}^{\mathrm{i}\xi x} \sum_{l=1}^{M} \left[\left(\tilde{H}_{r,pL}(\xi, 2\pi f) \tilde{P}_{l,L}(\omega) + \tilde{H}_{r,pR}(\xi, 2\pi f) \tilde{P}_{l,R}(\omega) \right) \mathrm{e}^{-\mathrm{i}\xi a_l} \right] \tag{6}$$

$$\begin{aligned} S_g(x, y, f; \omega) = \frac{1}{2\pi v} \mathrm{e}^{\mathrm{i}\xi x} \sum_{l=1}^{M} \Bigg[\Bigg(& \int_{-\infty}^{\infty} \tilde{H}_{g,L}(\xi, k_y, 2\pi f) \mathrm{e}^{\mathrm{i}k_x y} \mathrm{d}k_y \, \tilde{P}_{l,L}(\omega) \\ & + \int_{-\infty}^{\infty} \tilde{H}_{g,R}(\xi, k_y, 2\pi f) \mathrm{e}^{\mathrm{i}k_x y} \mathrm{d}k_y \, \tilde{P}_{l,R}(\omega) \Bigg) \mathrm{e}^{-\mathrm{i}\xi a_l} \Bigg] \end{aligned} \tag{7}$$

with $\xi = \frac{\omega - 2\pi f}{v}$.

The magnitude of the resulting response spectrum due to harmonic excitation is independent of the value of x. This reflects the fact that the spectrum represents the result of movement through the observation point of the steady-state wave field associated with the load moving along the x-axis from $x = -\infty$ to $x = \infty$. In the next section, stationary random roughness is assumed that is approximated as a sum of sinusoids. For each discrete harmonic component of this irregularity a moving harmonic force with a single angular frequency ω is generated at the wheel-rail contact point. For the case of constant moving loads, the relations in Eqs (2) and (3) can give the quasi-static response due to the moving axle loads of a train by setting the excitation frequency $\omega = 0$. For the simplified case where only a single rail and a single degree of freedom for each wheelset is considered in the model, the indices s and p can be omitted and only one term inside the brackets in Eqs (2), (3), (6) and (7) is taken into account.

(a) (b)

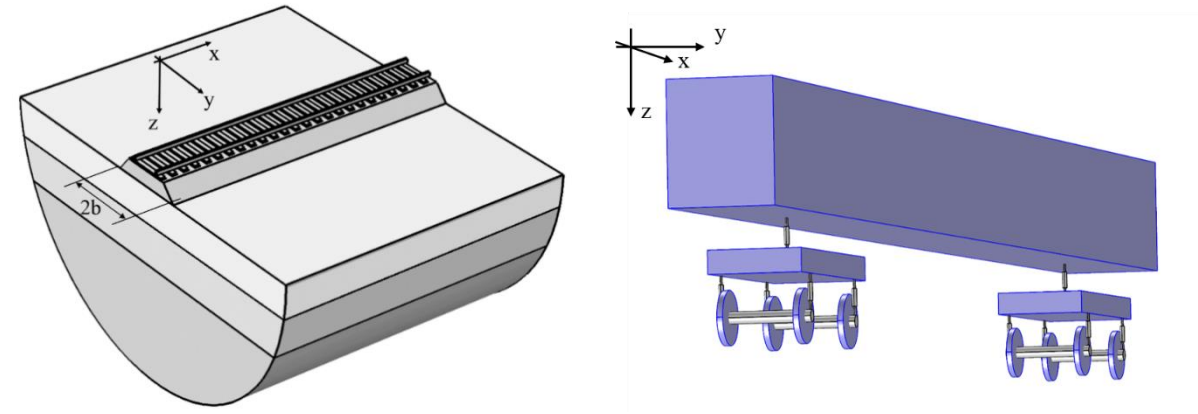

Figure 4. (a) The geometry of the track ground system; (b) three-dimensional multiple rigid-body vehicle system.

3.2 The coupled train-track system

For ground-borne vibration, where the frequency range of interest is usually between 2 and 250 Hz, the train is modelled as a linear multiple rigid-body system (see Figure 4(b)). In practice, due to the vehicle suspension, at frequencies above 10 Hz usually only the unsprung mass of the wheelsets is important. Consequently it is acceptable to neglect flexible modes of the car body. Only vertical interaction forces are considered and only the vertical dynamics of the sprung masses of the train are included. Since, as shown in Section 2, non-symmetric loading at the wheel/rail contact points occurs at relatively short wavelengths (high frequencies; usually above 10 Hz) the rolling modes of the car body and the bogie are not excited and thus each car body and bogie therefore can be further simplified by having only two degrees of freedom (DOFs), i.e., the vertical displacement of its mass centre and its pitch motion. Similarly, each wheel has only one DOF, i.e. its vertical displacement. In general, each train can have N_w wheels, N_b bogies and N_c car bodies resulting in $N = N_w + 2N_b + 2N_c$ DOFs. When both wheels of each wheelset (and both rails) are considered separately $N_w = 2M$, whereas for symmetric excitation the motion of each wheel and rail can be reduced to a single DOF and $N_w = M$. The coupling between vehicles is neglected.

In practice, the vehicle suspensions may have non-linear behaviour. However, to enable analysis in the frequency domain, here, each non-linear suspension is linearized, which is valid for small motion amplitudes. As a result, the equation of motion for the train is linear with constant coefficients and is specified by a mass matrix **M** and a stiffness matrix **K**. Viscous or viscoelastic damping can be introduced and included in the stiffness matrix, thus the elements of the stiffness matrix are complex and may be frequency dependent. The mass and stiffness matrices of several typical vehicles can be found in [18].

The vertical forces between the wheelsets and the rails, from the first to the last wheelset of the train, are denoted by $\boldsymbol{P}(t) = \{P_{1,s}(t),\ P_{2,s}(t), \dots, P_{M,s}(t)\}^{\mathrm{T}}$, where M is the number of the wheelsets, $s = L, R$ denotes the left and right rail as already used in Eqs (2) to (7) and the superscript T denotes the matrix transpose. The longitudinal co-ordinates of these forces are denoted by $a_1, a_2, \dots, a_M$. Each wheel-rail force can be divided into two components: one is the moving "quasi-static" load, i.e., the moving constant axle load, and the other is a moving dynamic load. The responses to the axle loads are independent of the vehicle dynamics. Only the dynamic wheel-rail forces are considered here; in the following, $\boldsymbol{P}(t)$ refers to these dynamic forces. The response to the quasi-static loads is also calculated but does not involve the dynamic wheel-rail interaction.

Assuming harmonic motion and setting $\boldsymbol{P}(t) = \widetilde{\boldsymbol{P}}(\omega)\mathrm{e}^{\mathrm{i}\omega t}$, and $\boldsymbol{w}_t(t) = \widetilde{\boldsymbol{w}}_t(\omega)\mathrm{e}^{\mathrm{i}\omega t}$ for the vector of displacements and rotations of the train, the equation of motion of the whole train is given by

$$-\omega^2\mathbf{M}\widetilde{\boldsymbol{w}}_t(\omega) + \widetilde{\mathbf{K}}\widetilde{\boldsymbol{w}}_t(\omega) = -\mathbf{L}\widetilde{\boldsymbol{P}}(\omega) \tag{8}$$

where $\widetilde{\mathbf{K}}$ denotes the dynamic stiffness matrix which may be frequency-dependent and $\mathbf{L} \in \mathbb{R}^{N\times N_w}$ is a matrix consisting of zeros and ones that maps the N_w excited DOFs of the wheels to the N DOFs of the train. The minus sign before $\widetilde{\boldsymbol{P}}$ indicates that the positive wheel-rail forces correspond to compression of the contact spring whereas positive displacements are downwards.

Denoting $\mathbf{R}_t(\omega) = (\mathbf{K} - \omega^2\mathbf{M})^{-1}\mathbf{L}$, the $N \times N_w$ complex matrix of receptances of the train DOFs due to forces at the wheels, Eq. (8) yields

$$\widetilde{\boldsymbol{w}}_t(\omega) = -\mathbf{R}_t(\omega)\widetilde{\boldsymbol{P}}(\omega) \tag{9}$$

The displacement vector of the N_w wheels produced by the wheel-rail forces is given by

$$\widetilde{\boldsymbol{w}}_w(\omega) = -\mathbf{R}_w(\omega)\widetilde{\boldsymbol{P}}(\omega) \tag{10}$$

where $\mathbf{R}_w(\omega)$ is the $N_w \times N_w$ complex receptance matrix at the wheels of the train given by

$$\mathbf{R}_w(\omega) = \mathbf{L}^{\mathrm{T}}(\mathbf{K} - \omega^2\mathbf{M})^{-1}\mathbf{L} \tag{11}$$

Similarly by denoting the rail receptance matrix of the track-ground system at the wheel-rail contact points in a moving frame of reference as $\mathbf{R}_r(\omega)$, the displacement vector at the wheel-rail contact points on the rails at frequency ω is given by

$$\widetilde{\boldsymbol{w}}_r(\omega) = \mathbf{R}_r(\omega)\widetilde{\boldsymbol{P}}(\omega) \tag{12}$$

Assuming that the wheel is always in contact with the rail, a linearized Hertzian contact spring with stiffness $k_{H,lp}$ can be inserted between the l-th wheelset and the p rail, although for the frequency range of ground-borne vibration, inclusion of the contact spring does not influence the total response significantly. The wheel/rail coupling is illustrated in Figure 5 for a model of a ballasted track, where

$\widetilde{w}_{w,lp}(\omega)$ denotes the displacement of the wheel and $\tilde{r}_{lp}(\omega)$ denotes the complex amplitude of the vertical profile of the p rail (rail irregularity) at the respective contact point. The vertical profile of the rail may be decomposed into a spectrum of discrete harmonic components. A single harmonic component is denoted by $r(x) = A\mathrm{e}^{\mathrm{i}(2\pi/\lambda)x}$ where λ denotes the wavelength and A the amplitude which may be complex (strictly the profile of the rail is the real part of $r(x)$). The relation between the angular frequency of the dynamic loading and the wavelength of the rail irregularity is $\omega = 2\pi v/\lambda$, where v is the velocity of the train.

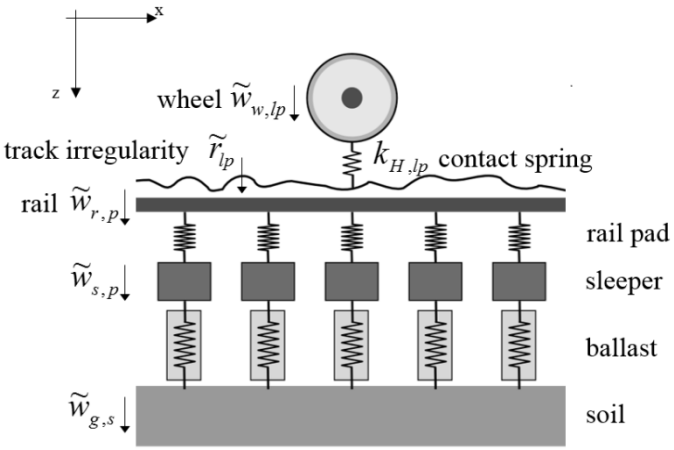

Figure 5. Coupling of a wheel with the track (rail, pad, sleeper, ballast) and the ground.

If the wheels on the p rail are all excited by the same unevenness then $\tilde{r}_{lp}$ is the same for each l except for a time lag:

$$r_{lp}(t) = A_p\mathrm{e}^{\mathrm{i}(2\pi/\lambda)(a_l+vt)} = A_p\mathrm{e}^{\mathrm{i}(2\pi/\lambda)a_l}\mathrm{e}^{\mathrm{i}(v/\lambda)t} \tag{13}$$

and thus the complex amplitude of the vertical profile is given as

$$\tilde{r}_{lp}(\omega) = A_p\mathrm{e}^{\mathrm{i}(2\pi/\lambda)a_l} = A_p\mathrm{e}^{\mathrm{i}(\omega/v)a_l} \tag{14}$$

If both rails and both wheels of each wheelset ($p = L, R$) are considered separately, the coupling at the (l, p) contact point is expressed by the relation

$$\widetilde{w}_{w,lp}(\omega) = \widetilde{w}_{r,lp}(\omega) + \tilde{r}_{lp}(\omega) + \tilde{P}_{l,p}(\omega)/k_{H,lp} \tag{15}$$

where $\widetilde{w}_{w,lp}(\omega)$ is the (l, p) element of the vector $\widetilde{\boldsymbol{w}}_w(\omega)$ in Eq. (10) and $\widetilde{w}_{r,lp}(\omega)$ is the (l, p) element of vector $\widetilde{\boldsymbol{w}}_r(\omega)$ respectively given in Eq. (12). Inserting these two equations into Eq. (15) yields

$$[\mathbf{R}_w(\omega) + \mathbf{R}_r(\omega) + \mathbf{R}_H]\widetilde{\boldsymbol{P}}(\omega) = -\tilde{\boldsymbol{r}}(\omega) \tag{16}$$

where $\tilde{\boldsymbol{r}}(\omega)$ is the vector that collects the vertical rail irregularity at all contact points (l, p) and $\mathbf{R}_H = \mathrm{diag}\{\frac{1}{k_{H,lp}}\}$ with $(l = 1,2, \dots, M; p = L, R)$ is the matrix of contact spring receptances.

Eq. (16) is a set of linear algebraic equations with the dynamic wheel-rail forces $\widetilde{\boldsymbol{P}}(\omega)$ as unknowns. Its solution will be used as an input for the coupled track-soil model to give the response of the rail (Eq. (6)) and of the ground in the free field (Eq. (7)).

3.3 Lateral discretization of the track-ground interface

The soil is modelled semi-analytically as a multi-layered half-space using the Fourier transform over wavenumber (k_x, k_y) with respect to the coordinates (x, y) [5]. The railway track is aligned in the x direction, with a geometry that is assumed invariant in the longitudinal direction, having a contact width $2b$ with the ground (see Figure 4(a)). Different railway structures including ballasted or slab track may be represented by different models having the same general form.

In the longitudinal direction, the two rails are represented as Euler-Bernoulli beams with mass and bending stiffness m_r and $E_r I_r$ per unit length of track respectively. The rail pads are modelled as distributed vertical stiffness k_p per unit length for each rail (see Figure 5 and 6(a)). The sleepers are modelled as a continuous mass per unit length of the track m_s, i.e. neglecting bending, and the ballast is modelled as continuous distributed vertical spring stiffness k_b with consistent mass m_b. An embankment, if present, can be modelled in the same way as the ballast. A similar model can be used for the case of a slab track by introducing an infinite Euler-Bernoulli beam with constant bending stiffness representing the slab and replacing the sleepers.

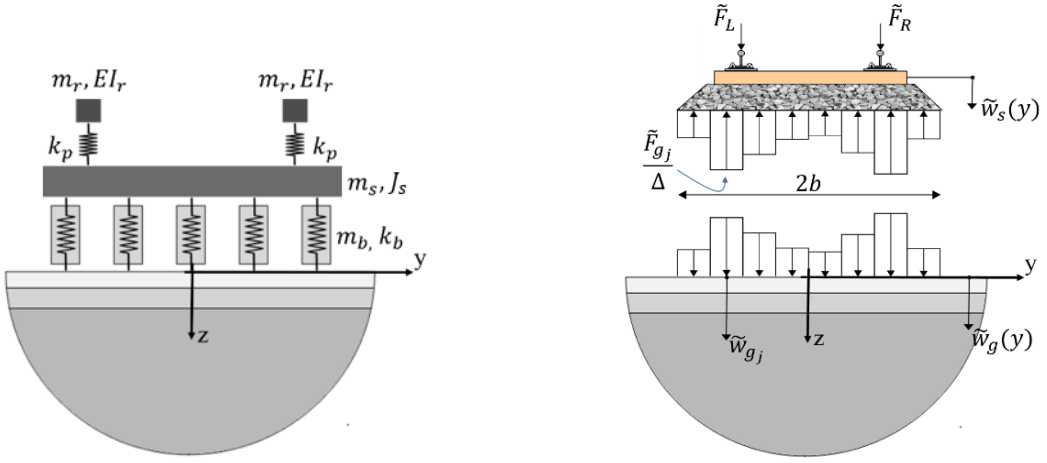

(a) (b)

Figure 6. (a) Lateral view of multibody model of the track; (b) discretization of the stress field across the track-ground interface.

The track exerts a distributed load on the half-space. To represent this, a contact force per unit length F_g between track and soil is introduced. In order to allow for an arbitrary load distribution across the width of the track, the interface conditions are discretised. The discretisation will introduce a finite sum of the normal tractions at the track/ground interface. The principle is shown in Figure 6(b). Across the

interface, discrete values y_j of the coordinate y are selected, positioned at the middle of a strip of width Δ. There are N_s such strips; within each strip j the stresses are assumed to be constant. Displacement compatibility is required along the lines $y = y_j$. The coordinate y_j is defined as $y_j = -b + \Delta\,(2j-1)/2$ where $1 \le j \le N_s$ with $N_s = 2b/\Delta$. For $N_s = 1$ a homogeneous stress distribution ensues, with displacement compatibility required along the centreline.

The displacement of a point on the ground within the j-th strip at wavenumber k_x can be calculated, using the Green's function for the layered half-space in a moving frame of reference, as the superposition of the displacements of that point due to the excitation at each strip, as follows

$$\widetilde{w}_g\left(k_x, y_j, \widehat{\omega}\right) = \sum_{i=1}^{N_s} \widetilde{H}_g\left(k_x, y_{ij}, \widehat{\omega}\right)\widetilde{F}_{gi} \tag{17}$$

where $\widetilde{H}_g\left(k_x, y_{ij}, \widehat{\omega}\right)$ is the response of a point at strip j, due to a unit harmonic excitation of frequency $\widehat{\omega} = \omega - k_x v$ at strip i, where $y_{ij} = y_i - y_j$ is the distance between strips i and j.

The transfer functions of the layered half-space are first calculated in the wavenumber domain, $\widetilde{H}_g\left(k_x, k_y, \widehat{\omega}\right)$; these are the Green's functions for a layered half-space due a unit load acting downwards at $y = 0$ and moving with speed v [5]. To calculate $\widetilde{H}_g\left(k_x, y_{ij}, \widehat{\omega}\right)$, therefore, the inverse Fourier transform from the k_y domain to the y domain should be calculated as

$$\widetilde{H}_g(k_x, y, \widehat{\omega}) = \frac{1}{2\pi}\int_{-\infty}^{\infty} \widetilde{H}_g\left(k_x, k_y, \widehat{\omega}\right)\mathrm{e}^{\mathrm{i}k_y y}\mathrm{d}k_y \tag{18}$$

The transfer function of the ground due to a strip load of width Δ and constant magnitude $1/\Delta$ per unit width, distributed symmetrically about $y = 0$, can be calculated by weighting $\widetilde{H}_g\left(k_x, k_y, \widehat{\omega}\right)$ by the factor $\frac{\sin\left(k_y\Delta\right)}{\Delta/2}$ corresponding to the transformation of the strip load to the wavenumber domain. Applying this to the j-th strip, and due to symmetry in the k_y domain, results in

$$\widetilde{H}_g\left(k_x, y_{ij}, \widehat{\omega}\right) = \frac{1}{2\pi}\int_{0}^{\infty} \widetilde{H}_g\left(k_x, k_y, \widehat{\omega}\right)\frac{\sin\left(k_y\Delta\right)}{\Delta/2}\cos\left(k_y y_{ij}\right)\mathrm{d}k_y \tag{19}$$

The integral in Eq. (19) can be calculated using a standard quadrature for each strip. The resulting system of equations for all strips in Eq. (17), dropping k_x and $\widehat{\omega}$ for brevity, can be written in matrix form as

$$\widetilde{\boldsymbol{w}}_g = \widetilde{\mathbf{H}}_g\widetilde{\boldsymbol{F}}_g \tag{20}$$

where the vectors $\widetilde{\boldsymbol{w}}_g$ and $\widetilde{\boldsymbol{F}}_g$ contain the displacements and forces respectively for all strips and $\widetilde{\mathbf{H}}_g$ is an $N_s \times N_s$ matrix of the form

$$\widetilde{\mathbf{H}}_g = \begin{bmatrix} \widetilde{H}_g(0) & \widetilde{H}_g(\Delta) & \cdots & \widetilde{H}_g((N-1)\Delta) \\ \widetilde{H}_g(\Delta) & \widetilde{H}_g(0) & \cdots & \widetilde{H}_g((N-2)\Delta) \\ \vdots & \vdots & \ddots & \vdots \\ \widetilde{H}_g((N-1)\Delta) & \widetilde{H}_g((N-2)\Delta) & \cdots & \widetilde{H}_g(0) \end{bmatrix} \tag{21}$$

3.4 The coupled track-ground system

By allowing the roll motion around the x axis (along the track centreline, Figure 6) for a rigid sleeper with polar moment of inertia J_s, the displacement of the sleeper can be written as a function of y as

$$\widetilde{w}_s(k_x, y) = \widetilde{w}_s(k_x) - y\tilde{\theta}_s(k_x) \tag{22}$$

where $\widetilde{w}_s(k_x)$ is the displacement of the centre of mass (at $y = 0$) of the sleeper and $\tilde{\theta}_s(k_x)$ is the angle of rotation around the x axis of the sleeper.

By considering discretised track-ground interface conditions of N_s strips, for the j-th strip the mutual force at the track/ground interface can be expressed, in the wavenumber-frequency domain, as

$$\begin{aligned} \tilde{F}_g(k_x, y_j) = \bar{k}_b\big(\widetilde{w}_s(k_x) - y\tilde{\theta}_s(k_x) - \widetilde{w}_{gj}(k_x, y_j)\big) \\ + \hat{\omega}^2 \frac{\bar{m}_b}{6}\big(\widetilde{w}_s(k_x) - y\tilde{\theta}_s(k_x) + 2\widetilde{w}_{gj}(k_x, y_j)\big) \end{aligned} \tag{23}$$

where and $\bar{k}_b = k_b/N_s$ and $\bar{m}_b = m_b/N_s$ are the stiffness and magnitude respectively of the ballast for any one strip when k_b and m_b are given as stiffness and mass per unit length of the track.

The above formulation allows the two rails to be included in the model separately. The force applied by each rail through the rail pad of stiffness k_p to the sleeper can be written as

$$\begin{aligned} \tilde{F}_{r,L}(k_x) &= k_p\left(\widetilde{w}_s(k_x) + b_r\tilde{\theta}_s(k_x) - \widetilde{w}_{r,L}(k_x)\right) \\ \tilde{F}_{r,R}(k_x) &= k_p\big(\widetilde{w}_s(k_x) - b_r\tilde{\theta}_s(k_x) - \widetilde{w}_{r,R}(k_x)\big) \end{aligned} \tag{24}$$

where b_r is half the track gauge and $\widetilde{w}_{r,L}(k_x)$, $\widetilde{w}_{r,R}(k_x)$ are the displacement of the left and the right rail respectively in the wavenumber domain.

Assembling the equations for the coupled track/ground system, assuming steady state harmonic solutions at circular frequency ω, gives a system of $N_s + 4$ algebraic equations

$$\begin{bmatrix} K_1(k_x) & 0 & -k_p & -k_p b_r & \mathbf{0}_{N_s}^{\mathrm{T}} \\ 0 & K_1(k_x) & -k_p & k_p b_r & \mathbf{0}_{N_s}^{\mathrm{T}} \\ -k_p & -k_p & K_2 & 0 & -K_3\mathbf{1}_{N_s}^{\mathrm{T}} \\ -k_p b_r & k_p b_r & 0 & K_4 & K_5\mathbf{y}_{N_s}^{T} \\ \mathbf{0}_{N_s} & \mathbf{0}_{N_s} & -K_3\mathbf{1}_{N_s} & K_5\mathbf{y}_{N_s} & K_6\mathbf{I}_{N_s} \end{bmatrix} \begin{Bmatrix} \widetilde{w}_{r,L}(k_x) \\ \widetilde{w}_{r,R}(k_x) \\ \widetilde{w}_s(k_x) \\ \tilde{\theta}_s(k_x) \\ \widetilde{\boldsymbol{w}}_g(k_x) \end{Bmatrix} = \begin{Bmatrix} P_L \\ P_R \\ 0 \\ 0 \\ -\widetilde{\boldsymbol{F}}_g(k_x) \end{Bmatrix} \tag{25}$$

where P_L, P_R are the loading on the left and right rail respectively; $\mathbf{y}_{N_s} = [y_1, \ldots, y_{N_s}]^{\mathrm{T}}$ is the vector that collects the N_s lateral discrete coordinates y_j of each strip; $\mathbf{0}_{N_s}$, $\mathbf{1}_{N_s}$ are vectors of N_s elements formed of zeros and ones respectively and $\mathbf{I}_{N_s}$ is the identity matrix of size $N_s \times N_s$. The quantities K_1, K_2, K_3, K_4 and K_5 are given as

$$\begin{aligned} K_1(k_x) &= E_r I_r {k_x}^4 - \widehat{\omega}^2 m_r + k_p \qquad K_2 = 2k_p + \bar{k}_b - \widehat{\omega}^2 \left(m_s + \frac{\bar{m}_b}{3}\right) \\ K_3 &= \left(\bar{k}_b + \widehat{\omega}^2 \frac{\bar{m}_b}{6}\right) \qquad K_4 = -\widehat{\omega}^2 J_s + k_p b_r - \sum_{j=1}^{N_s} \bar{k}_b \, y_j |y_j| \\ K_5 &= \left(\bar{k}_b - \widehat{\omega}^2 \frac{\bar{m}_b}{6}\right) \qquad K_6 = \left(\bar{k}_b - \widehat{\omega}^2 \frac{\bar{m}_b}{3}\right) \end{aligned} \tag{26}$$

Either hysteretic or viscous damping may be accounted for in the rail pad and the ballast by making the stiffness complex using a loss factor or a viscous damping constant in each case. The minus sign in the term $-\widetilde{\boldsymbol{F}}_g(k_x)$ on the right-hand side in Eq. (25) indicates that the force exerted at the bottom of the track structure by the ground is upward.

Substituting Eq. (20) into Eq. (25), $\widetilde{w}_{r,L}(k_x)$, $\widetilde{w}_{r,R}(k_x)$, $\widetilde{w}_s(k_x)$, $\tilde{\theta}_s(k_x)$ and $\widetilde{\boldsymbol{F}}_g(k_x)$ can be obtained for each wavenumber k_x. Once the contact force profile $\widetilde{\boldsymbol{F}}_g(k_x)$ has been calculated, it can be used as the excitation to the ground model in order to calculate the ground response $\widetilde{w}_{gj}(k_x, y)$ at a distance y from the origin. The total response at this point is then a superposition of its responses due to excitations at all the strips. The distance from the point to the j-th strip is $y - y_j$.

In terms of computational effort, the discretization of the track/ground interface involves the numerical calculation of the integral in Eq. (19) and the addition of one equation for each interface strip in the system of equations given in (25). This extra computational effort is significantly lower than that needed for the calculation of the transfer functions in the ground in the wavenumber domain $\widetilde{H}_{g,s}(k_x, k_y, \widehat{\omega})$. Moreover, the effect of the discretized interface in the ground response is directly related with the width of the interface strips and the wavelength of the Rayleigh waves in the ground. Consequently a limited number of strips is sufficient for the frequency range of interest of ground-borne vibration.

3.5 Results for non-symmetrical inputs on the two rails

In order to show the effect of phase differences between the loads on the two rails, Figure 7 shows the mobility in the free field for a railway system with a ballasted track on two different types of layered ground (Ground 1 and Ground 2) listed in Table 2 due to moving unit loads on both rails with different relative phase. These two layered half-space ground models have been used in [9] and although not based on actual sites, they are chosen as typical examples of what is likely to occur in practice. Both have a softer layer of depth 3 m overlying a stiffer half-space, the half-space being the same in the two cases for convenience. The track used for the simulations is a ballasted track largely based on the track

used in [19]. The width of the track/ground interaction strip is $2b$=3.2 m and the corresponding track parameters are listed in Table 3.

Table 2. The parameters used for different types of ground.

Parameters of ground	Ground 1 (soft ground)		Ground 2 (stiff ground)	
	Upper layer	Half-space	Upper layer	Half-space
P-wave speed (m/s)	240	700	500	700
S-wave speed (m/s)	120	350	250	350
Density (kg/m^3)	1800	2000	1800	2000
Young's Modulus (MPa)	69.12	653.3	300.0	653.3
Shear Modulus (MPa)	25.92	245.0	112.5	245.0
Poisson's ratio	0.333	0.333	0.333	0.333
Damping loss factor	0.1	0.1	0.1	0.1
Layer depth (m)	3.0	Infinite	3.0	Infinite

Table 3. Parameters used to represent the track

Rail	Bending stiffness per rail	$E_r I_r = 6.4$ MN m^2
	Mass per unit length per rail	$m_r = 60$ kg/m
	Damping loss factor	$\eta_r = 0.01$
	Track gauge	$b_r = 1.435$ m
Rail pad	Stiffness per rail per unit length	$k_p = 500$ MN/m^2
	Damping loss factor	$\eta_p = 0.1$
Sleeper	Mass per unit length	$m_s = 542$ kg/m
	Sleeper spacing	$\alpha = 0.6$ m
	Pitching moment of inertia around x per unit length	$J_s = 307$ kg m
Ballast	Mass per unit length	$m_b = 1740$ kg/m
	Stiffness per unit length	$k_b = 4640$ MN/m^2
	Damping loss factor	$\eta_b = 0.04$
	Ballast/ground interaction width	$2b = 3.2$ m

The transfer mobilities in Figure 7 are calculated with $N_s = 8$ strips at the track/ground loading interface. Three loading cases are considered: in the first case, the loads on the two rails are in phase ($\phi = 0$); in the second case, they are in antiphase ($\phi = \pi$); and in the third case their phase difference is $\phi = \pi/2$. For all three cases the speed of the load v is 250 km/h (69.44 m/s) and the response is shown at 8 m and 16 m from the track centreline.

For the case of symmetrical inputs (in phase, $\phi = 0$) and the softer soil a broad peak occurs in the transfer mobility at about 12 Hz. This corresponds to the cut-on frequency of the layered ground, above which waves propagate in the upper layer with little influence of the underlying half-space [1]. For the stiffer ground this cut-on frequency is at about 35 Hz. for the case of out-of-phase loading, the vibration

level is much reduced compared with in-phase loading. The difference between these two loading cases is similar for the two grounds and is greater at lower frequencies, gradually reducing above 40 Hz. For the case of $\pi/2$ phase difference in the loading, the response is about 3 dB lower than for the in-phase loading. This difference is found for all frequencies up to 60 Hz, for both distances and both types of ground.

Comparing Figures 7(a) and 7(c) for the soft ground with 7(b) and 7(d) for the stiff ground the mobilities are equal at low frequencies, where the transmission is dominated by the underlying half-space, this being identical for both grounds. The results start to differ at higher frequency, with the soft soil having higher mobility above 6 Hz where waves start to cut on in the upper layer of the soft soil.

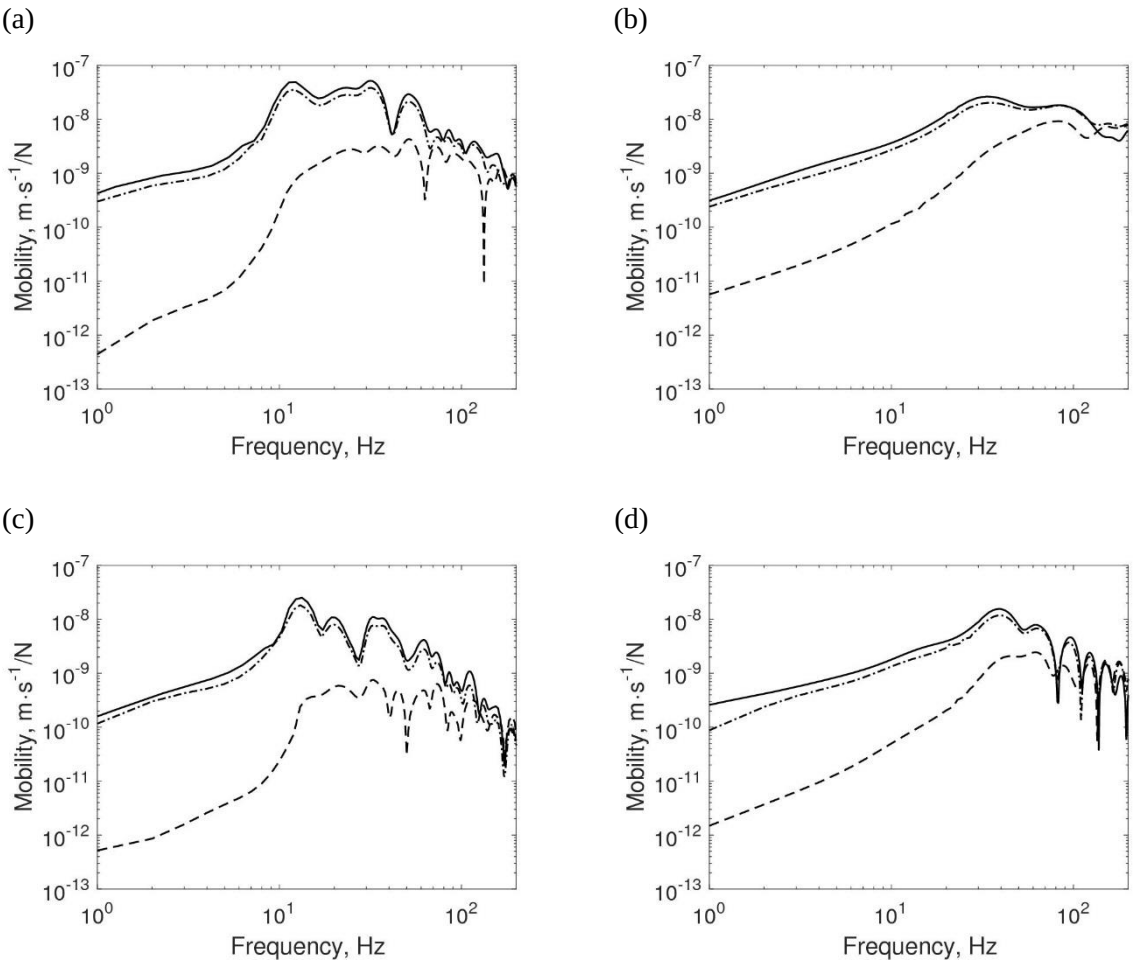

Figure 7. Response in the free field due to unit forces acting on both rails (a) at 8 m for soft soil; (b) at 8 m for stiff soil; (c) at 16 m for soft soil and (d) at 16 m for stiff soil: (−) $\phi = 0$; (− − −) $\phi = \pi$; (− · − ·) $\phi = \frac{\pi}{2}$.

3.6 Response spectrum due to track unevenness

In [18], by treating the rail unevenness as a random process, the formulation of the power spectrum of the ground surface response due to the rail irregularity is given for a point that is stationary as the train

moves past it. In this approach the motion of the train is included, which means that the response at a given frequency is a combination of responses induced by different excitation frequencies due to the Doppler effect in the ground. The expressions given in [18] are extended here to include the unevenness of both rails separately as well as the correlation between the two.

The vertical displacement spectrum of a point (x, y) on the ground surface due to a unit amplitude rail irregularity of wavelength λ, $w(x) = \mathrm{e}^{\mathrm{i}(2\pi/\lambda)x}$ on the s-th rail, is denoted by $S_s^0(x, y, f; \omega)$; where f is the frequency at which the spectrum is evaluated and ω is the excitation angular frequency determined by $\omega = 2\pi v/\lambda$.

At time t, the l-th wheelset is at $x = a_l + vt$, and the displacement input at the (l, p)-th wheel-rail contact point is given by Eq. (13). Thus, the vector of dynamic wheel-rail forces $\widetilde{\boldsymbol{P}}(\omega)$ in Eq. (16) due to the unit amplitude rail irregularity at all contact points $\tilde{r}_{lp}(\omega)$ can be calculated using Eq. (14) with $A_p = 1$. The elements of the receptance matrix $\mathbf{R}_r(\omega)$ in Eq. (16) are calculated using Eq. (2) by applying a single unit amplitude load $P_{l,s}(\omega) = 1$. Subsequently, $S_s^0(x, y, f; \omega)$ is obtained from Eq. (7) using the vector of forces $\widetilde{\boldsymbol{P}}(\omega)$ that is calculated due to the unit amplitude rail irregularity.

By assuming that a complete vertical rail profile can be represented by a large number of discrete wavenumber components k_n and that each harmonic component of the rail vertical profile is independent of the others, the double-sided power spectrum of the displacement at a fixed observation point in the free field can be calculated by

$$P_g(y, f) = 2|S(y, f; 0)|^2 + \frac{1}{2\pi}\sum_{n=1}^{M}[\boldsymbol{S}^0(y, f; \omega_n)^{\mathbf{T}}\mathbf{P}_{\mathrm{in}}(k_n)\boldsymbol{S}^0(y, f; \omega_n)^* + \boldsymbol{S}^0(y, f; -\omega_n)^{\mathbf{T}}\mathbf{P}_{\mathrm{in}}(k_n)\boldsymbol{S}^0(y, f; -\omega_n)^*]\Delta k_n \tag{27}$$

In the above expression the x coordinate is omitted since the response spectrum is independent of the value of x as shown in Section 3.1. The term $2|S(y, f; 0)|^2$ is the power spectrum generated by the quasi-static loads and is given by Eq. (7) using half the axle loads as the loads $\tilde{P}_{l,L}(0)$ and $\tilde{P}_{l,R}(0)$ for all M wheelsets. The term

$$\boldsymbol{S}^0(y, f; \omega_n) = \begin{Bmatrix} S_L^0(y, f; \omega_n) \\ S_R^0(y, f; \omega_n) \end{Bmatrix} \tag{28}$$

is a vector that collects the vertical displacement spectrum on the ground surface due to a unit amplitude irregularity of the left (L) and right (R) rail of wavelength $\lambda_n = 2\pi v/\omega_n$. Consequently, because of the symmetry about the track centreline $S_R^0(y, f; \omega_n) = S_L^0(-y, f; \omega_n)$.

In Eq. (27) the matrix

$$\mathbf{P}_{\mathrm{in}}(k_n) = \begin{bmatrix} \mathrm{P}_{\mathrm{LL}}(k_n) & \mathrm{P}_{\mathrm{LR}}(k_n) \\ \mathrm{P}_{\mathrm{RL}}(k_n) & \mathrm{P}_{\mathrm{RR}}(k_n) \end{bmatrix} \tag{29}$$

is the PSD matrix of the track vertical profile consisting of the auto-PSD (diagonal) and cross-PSD (non-diagonal) functions of the vertical profiles of the two rails where $k_n = n\Delta k$ and Δk denotes the spacing of the discrete wavenumbers. When the rail unevenness profiles of the two rails are considered to be fully correlated (the rails have the same vertical profile) all four elements of $\mathbf{P}_{\text{in}}$ are equal for each wavenumber. When the unevenness of the two rails is considered uncorrelated then the cross-PSD elements are zero.

The velocity power spectrum $\dot{P}_g(x, y, f)$, is then given by

$$\dot{P}_g(x, y, f) = (2\pi f)^2 \, P_g(x, y, f) \tag{30}$$

When divided by the time taken for the whole train to pass a fixed point, Eq. (27) and Eq. (30) give an estimate of the power spectrum of vibration displacement and velocity respectively at point (x, y) close to the track on the ground surface during the stationary part of the response [18].

4. Train pass-by response predictions

In this section, the model introduced in Section 3 is applied to investigate the effects of different loading conditions at the track and different interface conditions between the track and the ground. In particular, results are compared between the response that is calculated by assuming a fully correlated and in-phase unevenness applied on both rails and the response obtained by assuming that the unevenness on the two rails is uncorrelated. The results of those two assumptions are compared with the case in which the actual rail unevenness as measured by a TRC is used as input for the model.

The response is calculated for the full pass-by of a train at 250 km/h (69.44 m/s). The train is modelled as a number of linear multibody systems that represent the vehicles as described in Section 3.2 and shown in Figure 8. When the loading due to the rail unevenness is applied separately on each rail and the two rails have different responses, the rotational properties of the track and wheelset are included by considering the moment of inertia of the sleeper J_s and the wheelset J_w around the x axis.

The ballasted track with properties given in Table 3 is used for all simulations; two different types of layered ground are considered with the properties listed in Table 2. The train parameters used correspond to those used in [20]. Unlike [20] a four-car train consisting of identical vehicles is used with a total length of 106.4 m. The parameters are listed in Table 4, see also Figure 8. The values of the dynamic stiffness due to viscous damping for primary and secondary suspensions are $k_p = k_p^{'} + i\omega c_p$ and $k_s = k_s^{'} + i\omega c_s$ respectively.

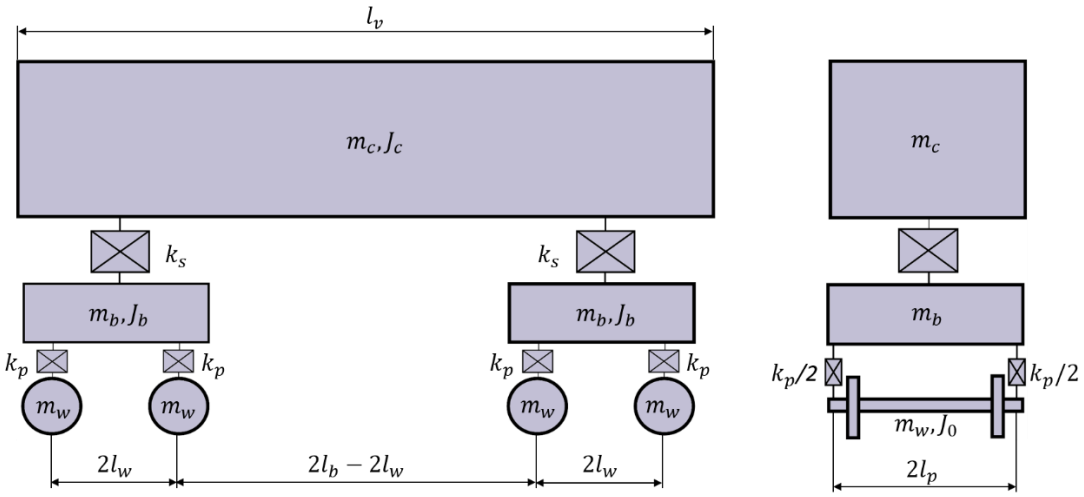

Figure 8. A vehicle model with primary and secondary suspensions.

Table 4. Vehicle parameters used [20].

Car body	Mass	$m_c = 40000$ kg
	Pitching moment of inertia	$J_c = 2 \cdot 10^6$ kg · m^2
	Overall vehicle length	$l_v = 26.6$ m
Bogie	Mass	$m_b = 5000$ kg
	Pitching moment of inertia	$J_b = 6000$ kg · m^2
	Half distance between bogie centres	$l_b = 9.5$ m
Wheelset	Mass	$m_w = 1800$ kg
	Roll moment of inertia	$J_w = 600$ kg · m^2
	Half distance between axles	$l_w = 1.35$ m
	Contact stiffness (per wheel)	$k_H = 1.46$ GN/m
	Total axle load	$P = 140.1$ kN
Primary suspension	Vertical stiffness per axle	$k_p' = 2.4$ MN/m
	Vertical viscous damping per axle	$c_p = 30$ kN · s/m
	Lateral half distance between springs	$l_p = 0.8$ m
Secondary suspension	Vertical stiffness per bogie	$k_s' = 0.6$ MN/m
	Vertical viscous damping per bogie	$c_s = 20$ kN · s/m

4.1 Track and wheel receptances

Prior to showing response predictions it is instructive to consider the receptances of the wheel and track that are combined with the unevenness to give the interaction forces, as shown in Eq. (16). Figure 9 shows the magnitude and the phase of the track receptance in a moving frame of reference at the speed of 250 km/h. Corresponding results for the wheel receptance are also shown. In each case, the track is coupled to the ground via $N_s = 8$ strips across the whole width of the track. The results in Figures 9(a) and 9(b) correspond to a symmetrical loading case where identical loads of amplitude 0.5 N are applied to both rails (and both wheels). This results in only translational motion of the sleeper and thus the two rails have identical response. For this case the track model can be simplified to a single combined rail/railpad with the sleepers represented only by their mass. For comparison, results are given in Figures

9(c) and 9(d) in which a unit load is applied to one of the two rails. The sleeper and the wheelset are now free to rotate. The receptance shown corresponds to the rail (and wheel) that are excited.

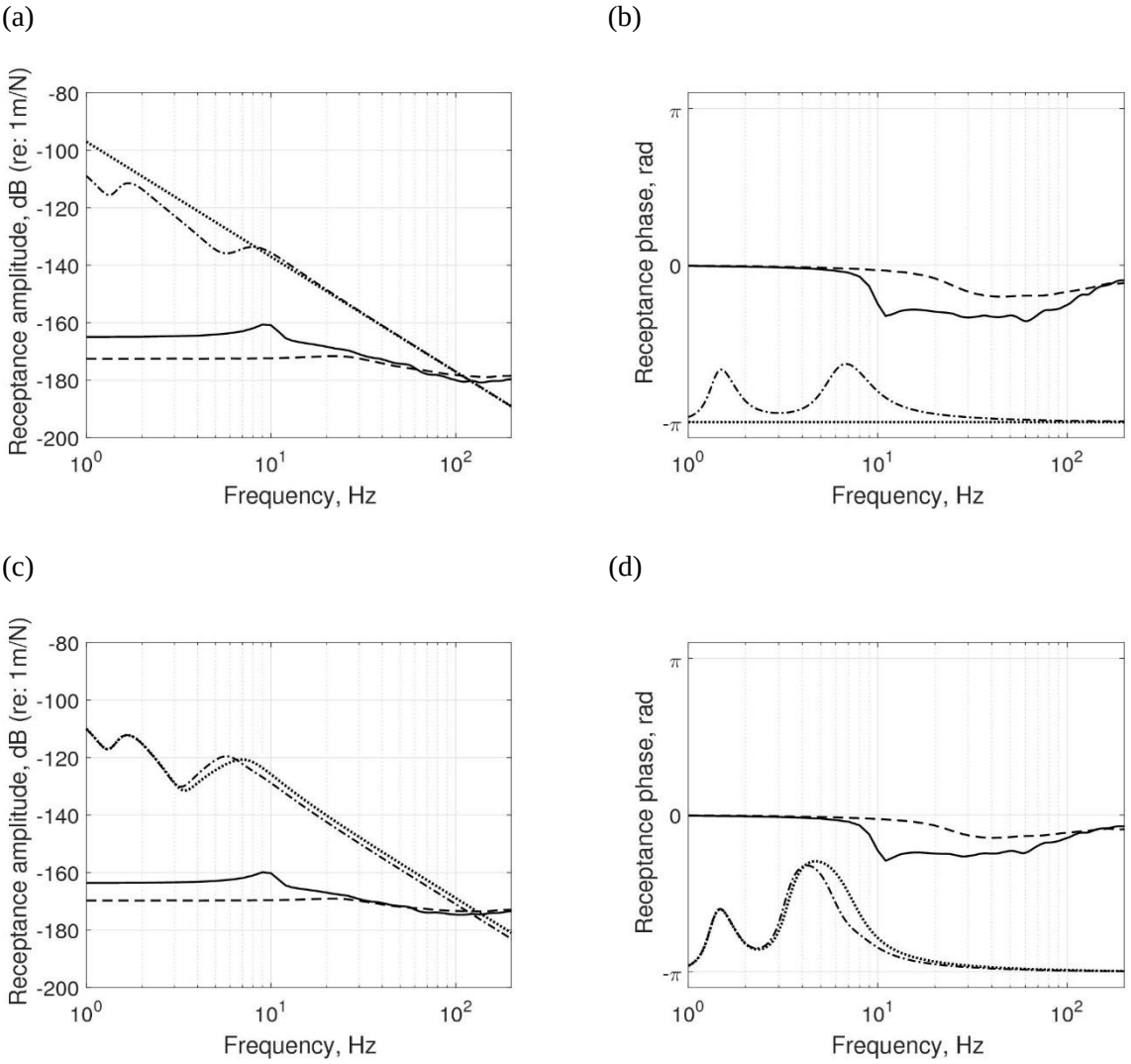

Figure 9. Track point receptance magnitude and phase: (−) on soft soil; (− − −) on stiff soil and wheel point receptance magnitude and phase: (a) - (b): track and wheelset excited symmetrically (load of 0.5 N on both rails/wheels), (− · − ·) full vehicle; (····) unsprung mass only. (c) - (d) excitation on one rail and wheel, (− · − ·) $J_w = m_w b_r^2/4$; (····) $J_w = 600$ kg · m^2.

Although the two layered grounds show different track receptances (by up to 12 dB) at lower frequencies, above 30 Hz the track stiffness dominates the response and the receptance values have the same level of magnitude. Comparing the results in Figures 9(a) and 9(c) the track receptances are similar at low frequencies but above approximately 40 Hz the receptance of the single rail becomes larger than that when both rails are excited, with the difference increasing to about 5 dB by 100 Hz. At frequencies where the beam response dominates, the difference between a single rail and composite beam representing two rails is expected to be 6 dB.

The wheel receptance magnitude and phase are also shown for comparison in Figure 9. In the results shown in Figures 9(a) - (b), only the vertical dynamics of the wheelsets are taken into account. Due to the symmetry of the loading, both wheels have the same displacement and no rotation of the wheelset is included, resulting in a vehicle model with 10 DOFs. For comparison, in Figures 9(a) - (b), a second model is shown consisting only of the unsprung masses; thus the whole vehicle is modelled with only four independent DOFs. In the latter case the wheel receptance matrix $\mathbf{R}_w$ in Eq. (11) is a diagonal matrix with elements $r_{kk}^w(\omega) = -1/(m_w\omega^2)$.

The wheel receptance values shown in Figures 9(c) - (d) are from the same model when the rotation of the wheelsets is taken into account, resulting in a vehicle model with 14 DOFs. Two cases are shown. In the first, the value of the roll moment of inertia of the wheelset is selected to be $J_w = \frac{1}{4}m_w b_r^2 = 927\ \text{kg}\cdot\text{m}^2$, where m_w is the mass of the wheelset (see Table 4) and b_r is the track half-gauge (see Table 2). For this value of the moment of inertia, if the free wheelset was excited at one wheel the other wheel would have no motion. Nevertheless, due to connection via the suspension to the bogie, which is constrained not to roll, there is still some coupling between the two sides. The second case in Figures 9(c) - (d), has a smaller moment of inertia $J_w = 600\ \text{kg}\cdot\text{m}^2$ as given in Table 4.

In Figure 9(a), as expected, the results for the 10 DOF model are identical to those for the unsprung mass above 10 Hz whereas at lower frequencies the effects of the vehicle bouncing and pitching resonances can be seen. This resonant behaviour is modified by inclusion of the roll motion of the wheelset as seen in Figure 9(c). For low frequencies up to 2 Hz the results are unaffected but in the frequency range 2 Hz to 10 Hz the receptances from the various models show differences due to the influence of the inertia of the wheelsets and the interaction with the vehicle's sprung mass through the primary suspension. For frequencies above 10 Hz, the wheel receptance of the two 14 DOF models is 6 dB or 8 dB higher than the 10 DOF model due to the added flexibility introduced by the roll motion of the wheelsets. As expected, the model with the lower roll moment of inertia has a 2 dB higher receptance for all frequencies above 10 Hz.

For symmetric loading, as in Figure 9(a), the frequency at which the receptances of the wheelset and the track have equal magnitude is referred to as the unsprung-mass-on-track-stiffness resonance [1]. At this resonance frequency the wheelset and the rails are moving vertically and in-phase on the track stiffness and the interaction force has a maximum. This resonance frequency can be identified in Figure 9(a) at around 120 Hz for the soft ground and slightly lower at 108 Hz for the stiff ground. In Figure 9(c), the corresponding frequency where the receptances of the wheel and the track on soft ground are equal occurs at around 120 Hz for the case of the vehicle with $J_w = 927\ \text{kg}\cdot\text{m}^2$ and around 138 Hz for the case of the vehicle with $J_w = 600\ \text{kg}\cdot\text{m}^2$. For the stiff ground the corresponding frequencies are 115 Hz and 130 Hz respectively.

4.2 Ground vibration due to the passage of the train

The unevenness PSD that is used as an input for all train pass-by simulations in this section is from the ballasted track reported in [14] and shown in Figure 10. Both rail profiles were acquired with a track recording coach that measured the loaded profile of the track. Figure 10 shows the auto-PSD of the unevenness of the two rails; that is the diagonal elements of matrix $\mathbf{P}_{\text{in}}$ in Eq. (29). Analysis parameters are listed in Table 1. The values are given with respect to wavenumber and to frequency for train speed of 250 km/h. The corresponding spectra of rail unevenness expressed in one-third octave band form are given in Figure 1(a).

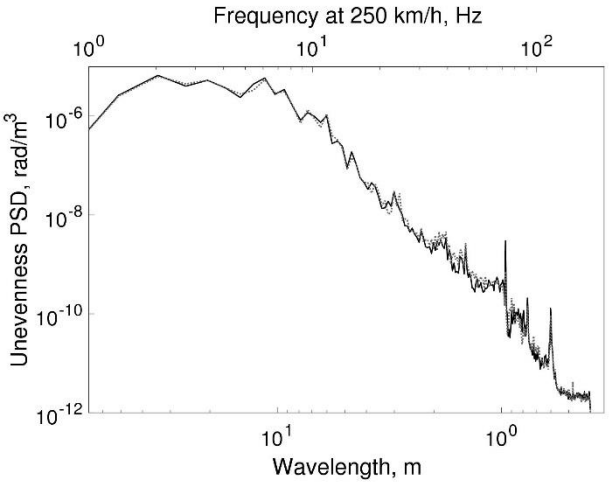

Figure 10. Track unevenness PSD obtained from Steventon site [14] of (−) the left rail and (····) the right rail.

For completeness, Figure 11(a) shows the ratios of the cross-PSD to the auto-PSDs of the unevenness of the two rails; that is the ratio of the off-diagonal elements of matrix $\mathbf{P}_{\text{in}}$ in Eq. (29) to the diagonal elements. Figure 11(b) shows the relative (cross-PSD) phase between the left and right rail profiles. The values are given with respect to wavenumber and to frequency for train speed of 250 km/h. It can be seen in Figure 11 that at wavelengths longer than 4 m (or at frequencies lower than 20 Hz) the ratios of the PSDs is close to 1 and the phase is close to zero, indicating that there is strong correlation between the two rails.

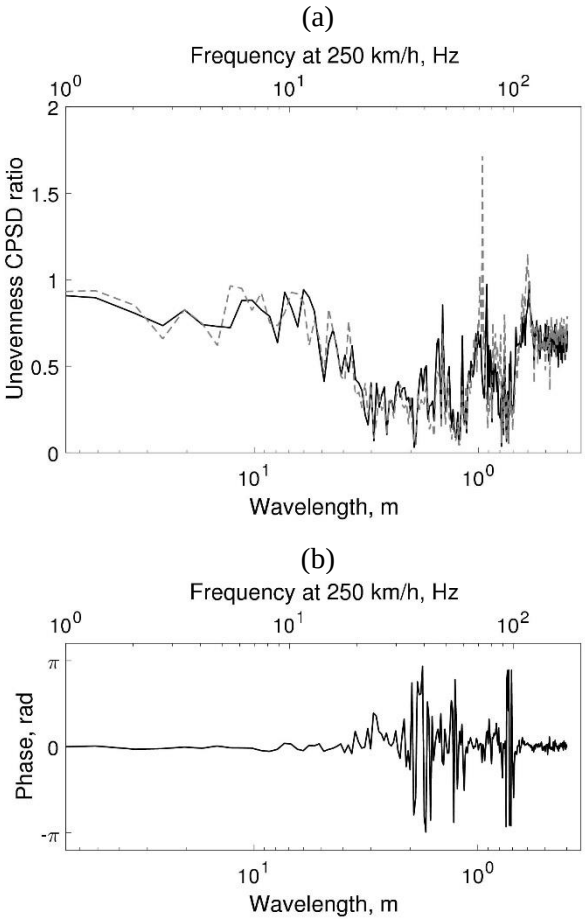

Figure 11. Track unevenness obtained from Steventon site [14]: (a) cross-PSD over auto-PSD ratio of (−) the left rail and (····) the right rail; (b) relative phase between the rails unevenness.

This unevenness spectrum is introduced into the model described in Section 3, first assuming symmetric loading of the two rails based on the average spectrum of the two rails shown in Figure 10. The predicted contact force spectrum of the leading and the trailing wheelsets of the first bogie due to excitation by track unevenness is shown in one-third octave form in Figure 12 for the two ground types. These are calculated using Eq. (16) and are shown as the force per wheel. At low frequency, where the vehicle receptance is much greater than that of the track (see Figure 9(a)), the contact force is independent of the track receptance and thus the results for the two grounds are identical. At higher frequency this no longer holds. Here, the vehicle receptance is mass-controlled while the track receptance is stiffness-controlled. As noted in Figure 9(a), these have equal magnitude at around 110 - 120 Hz, which is identified as the coupled vehicle-track resonance and corresponds to a peak in the contact force. The results for the trailing wheelset can be seen to be higher than for the leading wheelset between 2.5 and 8 Hz.

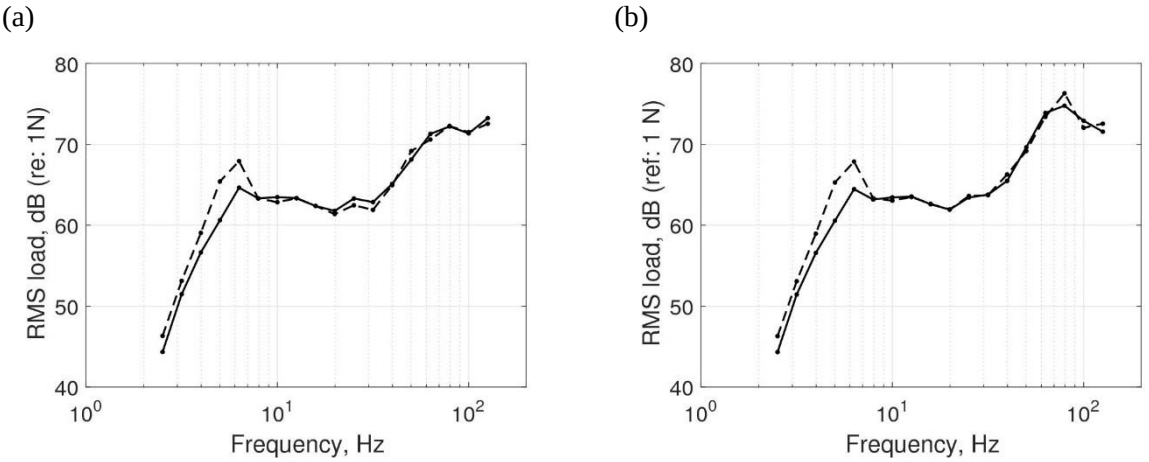

Figure 12. Dynamic wheel/rail contact force (per wheel) in one-third octave bands for the (a) soft ground and (b) the stiff ground: (−) leading wheelset and (− − −) trailing wheelset of the leading bogie.

The vertical vibration velocity level at the ground surface due to the passage of the train is shown in Figure 13. The results are calculated using the method described in Section 3.7 and are expressed as the average one-third octave band spectrum at certain distances from the track centreline during the train pass-by. The vibration due to both the moving quasi-static load and the dynamic load is calculated; the graphs show the total vibration level and that due to the dynamic excitation. Results are shown at 8 m and 16 m from the track. The response is calculated using symmetric loading. For this case the unevenness profile is identical for the two rails and thus it can be considered as fully correlated inputs. The results are based on the case where the track/ground interface is split into $N_s = 8$ strips.

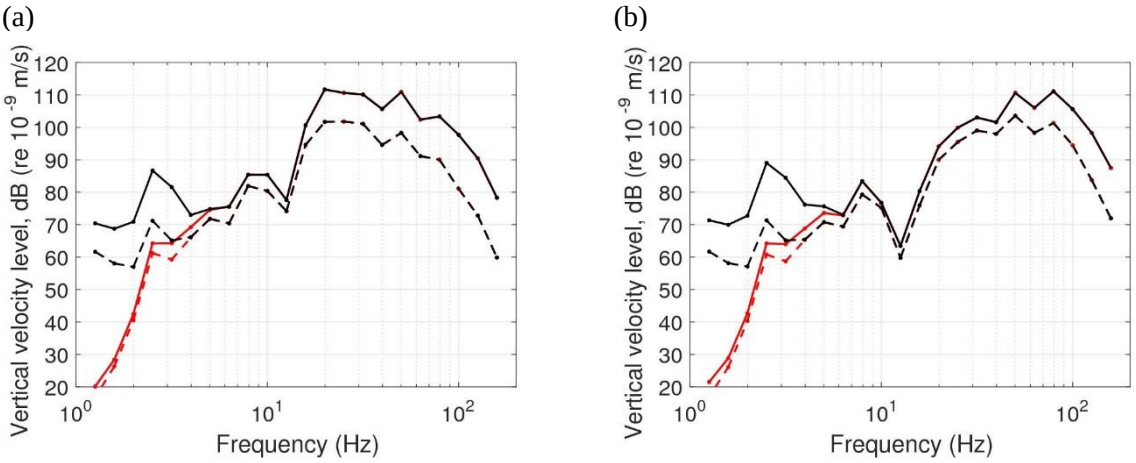

Figure 13. Total (black lines) and dynamic (red lines) ground response level in one-third octave bands of (a) soft soil and (b) stiff soil: (−) 8 m; (− − −) 16 m from the track for fully correlated inputs at the two rails.

Comparing the total vibration response for both ground types with the dynamic vibration response in Figure 13, it can be seen that the dynamic component dominates the response at frequencies above 4 Hz. Below 4 Hz, where the quasi-static response is significant, the response is similar for the two ground types. Above 4 Hz the responses calculated for the two ground types start to differ, with the soft ground

showing higher levels of vibration, and this difference is more prominent at 6 Hz and above. This is consistent with Figure 7 which shows that the mobilities are equal for the two ground types at low frequencies, where the transmission is dominated by the underlying half-space. Above 6 Hz the soft ground shows higher vibration levels (up to 20 dB at 16 Hz, close to the cut-on frequency of the soft ground, see Figure 7). At higher frequency, above 50 Hz for 8 m and 35 Hz for 16 m, the soft ground shows lower vibration levels due to a greater influence of damping since the wavelengths in the soil are shorter.

4.3 Comparison for different vehicle-track-ground loading conditions

Figure 14 and Figure 15 show the effect of various assumptions on the vertical wheel/rail contact force of the leading axle (leading bogie) and the ground vertical vibration level respectively. The results for the contact force are shown as the level difference in dB relative to the contact force shown in Figure 12 for both the soft and the stiff ground. The results for the ground vibration level are shown as the level difference in dB relative to the vibration level shown in Figure 13 for both the soft and the stiff ground at 8 m and 16 m from the track.

Figure 14, shows the effect of the number of strips considered between the track and the ground. Results for a single strip ($N_s = 1$) are compared with the nominal case of $N_s = 8$ strips. Figure 14(a) shows that the contact force is almost independent of the number of strips used for the track/ground loading ($N_s = 1$ and $N_s = 8$) for both ground types. In Figure 14(b) it can be seen that, for the soft ground, using a uniform track/ground loading distribution underestimates the predicted vibration level compared with the nominal case by up to about 3 dB at 40 Hz for a distance of 8 m and at 31.5 Hz for 16 m from the track. For the stiff ground the difference between the two predictions occurs at a higher frequency, with the maximum underestimation of 5 dB at 80 Hz for 8 m from the track.

Figure 15(a) shows the changes in the contact force and Figure 15(b) shows the changes in the ground response that occur when only the unsprung mass of the vehicle is considered compared with the nominal model based on the 10 DOF vehicle model. As expected from the wheel receptances shown in Figure 9(a), the differences between the two models occur mainly in the frequency range below 10 Hz where the dynamics of the sprung mass and the suspension contribute to the wheelset response. For both cases Figure 15 show differences of up to around 8 dB. In Figure 15(b), below 2 to 3 Hz the total response is dominated by the quasi-static excitation which is independent of the dynamic properties of the vehicle.

(a) (b)

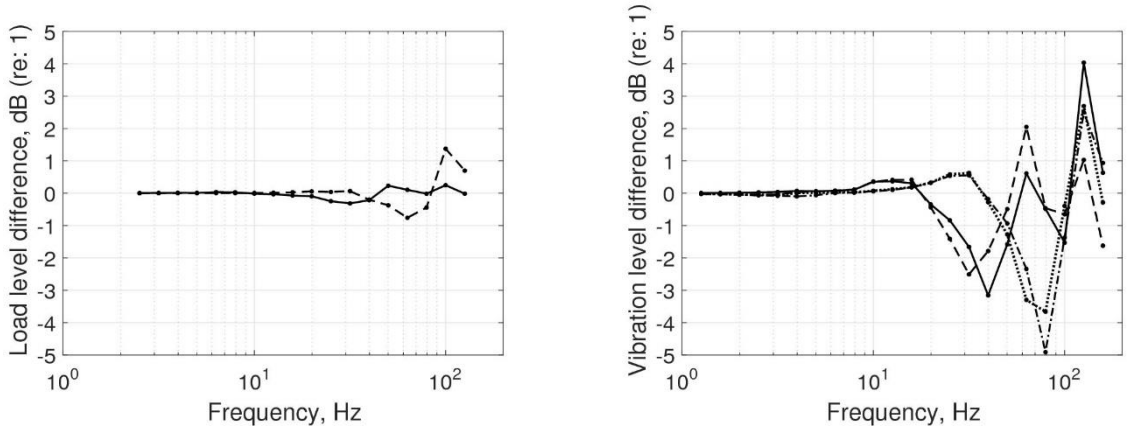

Figure 14. One-third octave spectra level difference between the nominal model and the model with $N_s = 1$ strip for (a) wheel/rail contact force of the leading axle: $(-)$ soft ground; $(- - -)$ stiff ground and (b) ground vibration level: $(-)$ soft ground 8m; $(- - -)$ soft ground 16 m; $(- \cdot - \cdot)$ stiff ground 8m; $(\cdots)$ stiff ground 16 m from the track.

(a) (b)

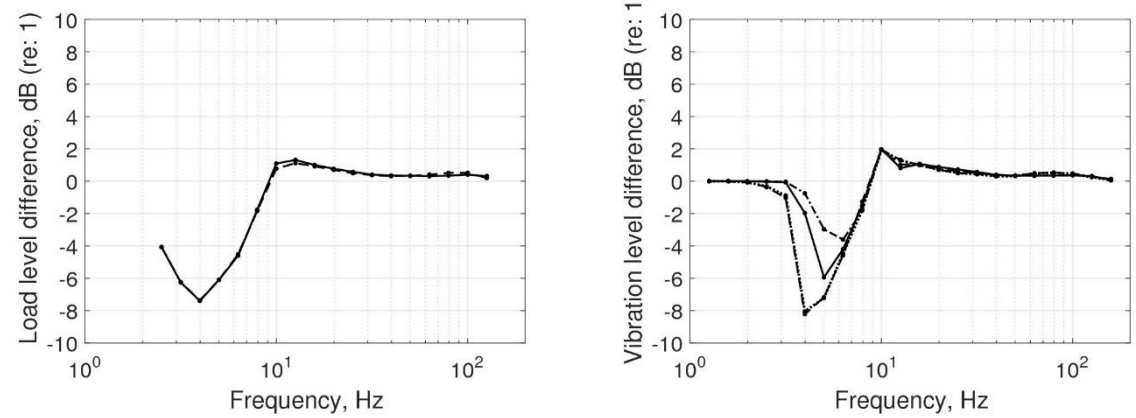

Figure 15. One-third octave spectra level difference between the nominal model and the model with $N_s = 8$ strips and unsprung mass only for (a) wheel/rail contact force of the leading axle: $(-)$ soft ground; $(- - -)$ stiff ground and (b) ground vibration level: $(-)$ soft ground 8m; $(- - -)$ soft ground 16 m; $(- \cdot - \cdot)$ stiff ground 8m; $(\cdots)$ stiff ground 16 m from the track.

4.4 Comparison for different level of unevenness correlation between the rails

Finally, the difference in model predictions is shown between the nominal fully correlated (symmetric) model and the models in which: (i) the rail unevenness is considered to be uncorrelated on the two rails and (ii) the rail unevenness is considered to be partially correlated as measured. In both these cases, the track is modelled using both rails with the sleeper and wheelsets allowed to rotate around the axial direction. In each case results are shown for the two values of wheelset roll moment of inertia $J_w = 927\ \text{kg} \cdot \text{m}^2$ and $J_w = 600\ \text{kg} \cdot \text{m}^2$ as discussed in Section 4.1. The same unevenness spectrum shown in Figure 10 is used in each case.

In Figure 16, the difference in force spectra is shown. Since the measured rail unevenness is different between the two rails, the level difference shown in Figure 16 is calculated using the average force spectrum predicted for the two contact points of the leading wheelset. Nevertheless, the difference in the contact force between the two wheels of each axle is small.

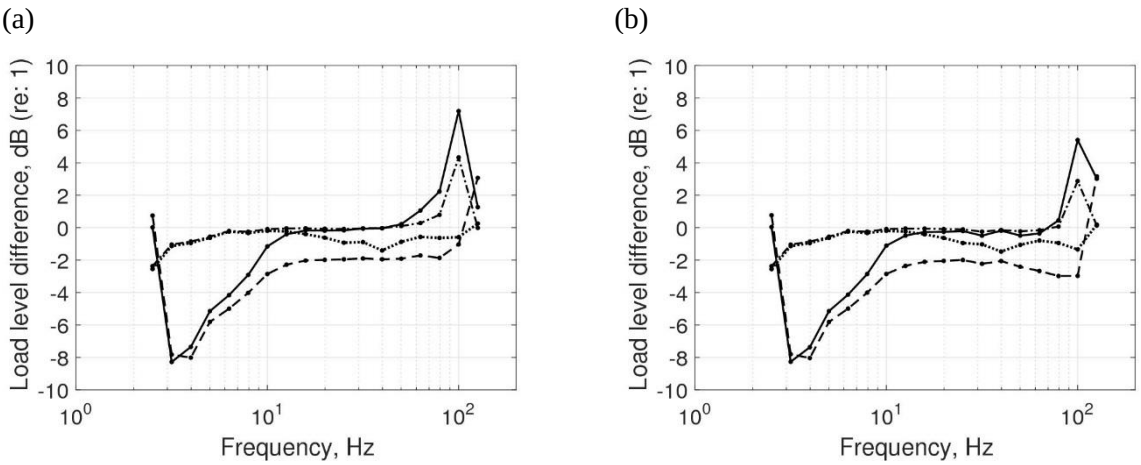

Figure 16 One-third octave spectra level difference of wheel/rail contact force of the leading axle for (a) the soft ground and (b) the stiff ground. Differences are shown between the nominal model and models with (−) uncorrelated unevenness and $J_w = 927$ kg · m^2; (− − −) uncorrelated unevenness and $J_w = 600$ kg · m^2; (− · − ·) partially correlated unevenness and $J_w = 927$ kg · m^2 and (····) partially correlated unevenness and $J_w = 600$ kg · m^2.

In Figure 16 the models with uncorrelated unevenness show much lower force levels in the frequency range 3 - 12 Hz, with a maximum difference of 8 dB at 3 Hz. These large differences are due to the rotational motion of the wheelsets, as seen in the wheel mobilities in Figure 9. However, these differences should not affect the predicted total ground response since at the lower frequencies this is dominated by the quasi-static excitation. In the frequency bands 12.5 to 50 Hz the model with $J_w = 927$ kg · m^2 shows similar force level to the fully correlated model. Above 50 Hz this model starts to show higher contact forces, with a maximum at 100 Hz due to the resonance of the wheelset rotation on the track stiffness. The model with $J_w = 600$ kg · m^2 shows a similar trend but it is about 2 dB lower the peak occurs at a higher frequency.

The models with partially correlated unevenness according to the measurements show similar force levels with the fully correlated model for frequencies below 50 Hz. Above 50 Hz for the model with $J_w = 927$ kg · m^2 (and 80 Hz for the model with $J_w = 600$ kg · m^2) the force shows similar trends with the uncorrelated cases.

Figure 17 shows the effect of the different model assumptions described above on the predicted vertical velocity levels. The results are shown as the level difference in dB relative to the total ground response shown in Figure 13. In each case, results are shown for both the soft and the stiff ground at 8 m and 16 m from the track. Similar to the contact force results shown in Figure 16, in both these cases, the track

is modelled using both rails with the sleeper and wheelsets allowed to rotate around axial direction. For consistency, in both models the track/ground coupling is based on $N_s = 8$ strips. Results are given for two values of the wheelset roll moment of inertia, as discussed in Section 4.1.

Below 4 Hz the response is dominated by the quasi-static excitation so the correlation of the dynamic loads does not affect the response.

For the cases where uncorrelated excitation is assumed on the two rails, above 4 Hz and up to 63 Hz for the model with $J_w = 927\ \mathrm{kg \cdot m^2}$ (and 80 Hz for the model with $J_w = 600\ \mathrm{kg \cdot m^2}$) the response predicted in one-third octave bands is a constant value of 3 dB lower than the case of the symmetric (fully correlated) loading. This difference is to be expected if one considers that the PSD matrix $\mathbf{P}_{\mathrm{in}}$ in Eq. (29) for the fully correlated case consists of non-zero and equal elements while for the uncorrelated case the non-diagonal elements are zero. Accordingly, the total power spectrum $P_g(y, f)$ in Eq. (27) for the fully correlated case should have double magnitude than for the uncorrelated inputs case. This ratio of 2 in the predicted power spectrum corresponds to a difference of 3 dB in the one-third octave band vibration levels.

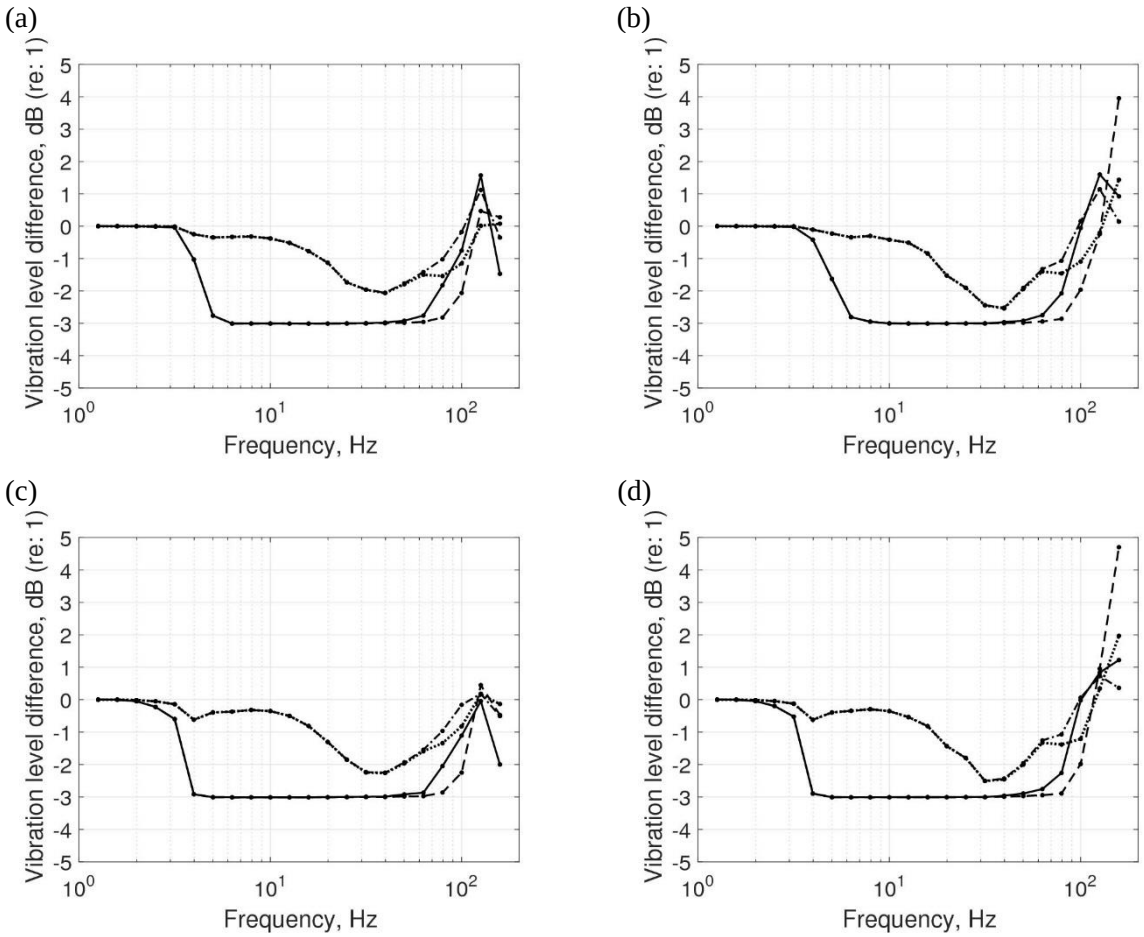

Figure 17. Ground vibration level difference in one-third octave bands (a) at 8 m from the track for soft ground, (b) at 8 m from the track for stiff ground, (c) at 16 m from the track for soft ground and (d) at 16 m from the

track for stiff ground. Differences are shown between the nominal model and (a) (−) uncorrelated unevenness and $J_w = 927$ kg · m^2; (− − −) uncorrelated unevenness and $J_w = 600$ kg · m^2; (− · − ·) partially correlated unevenness and $J_w = 927$ kg · m^2 and (····) partially correlated unevenness and $J_w = 600$ kg · m^2.

For the cases with correlated but not symmetric unevenness the predictions show that the response has similar levels with the fully correlated case for frequencies below 20 Hz which for train speed of 250 km/h correspond to excitation due to unevenness wavelengths that are longer than about 4 m (see Figure 11). Above 20 Hz the vibration levels decrease and tend to the -3 dB value of the uncorrelated case. These results are consistent with the cross-PSD ratio magnitude given in Figure 11(a) and show that the weaker correlation between the rail unevenness of the two rails that appears for wavelengths longer than about 4 m leads to lower vibration levels in the free field that can be up to 3 dB.

At high frequency the response increases notably for all the non-symmetric loading cases. Similarly with the increase in the force level shown in Figure 16, the increase in the ground vibration can be attributed to the effect that the additional rotational modes of the wheelset on the track stiffness are excited. For symmetric loading these rotational modes of the wheelset are not excited and thus the predicted ground response is lower than when the rail unevenness on the two rails is treated as uncorrelated. Similar results are shown when a different value of wheelset moment of inertia is used, the main differences being above 80 Hz.

5. Conclusions

A model has been established for the vibration due to surface railways that operates in the wavenumber-frequency domain and takes into account the traction variation across the track-ground interface and includes rotation of the sleepers and wheelsets about the axial direction. This allows investigations of the effect of the level of correlation between the unevenness on the two rails.

The extent to which the unevenness of the two rails is correlated has been estimated from measurements of track geometry obtained with track recording vehicles for four tracks of different types and operational standards. The results showed that for unevenness wavelengths longer than about 3 m the unevenness of the two rails can be considered to be strongly correlated (and in phase). At shorter wavelengths the unevenness of the two rails should be treated as uncorrelated inputs.

It is shown that it is important to include the traction variation across the track-ground interface in the model when determining the vibration in the free field, even for symmetric loading. This is due to the fact that, for certain excitation frequencies, the width of the track is equal to the wavelength of Rayleigh waves in the surface layer resulting in an underestimation of the response if a constant traction is assumed.

Train pass-by simulations from the developed model showed that when the unevenness of the two rails is treated as uncorrelated the dynamic component of the ground response is 3 dB lower than when the

unevenness is assumed identical on the two rails for frequencies up to 50 Hz. Moreover, when the unevenness of the two rails is not symmetrical the rotational modes of the wheelset on the track stiffness are excited and the predicted response level of the vibration in the free field can be notably greater in the frequency bands around 100 Hz than when the unevenness is assumed identical on the two rails.

ACKNOWLEDGEMENTS

This work is undertaken as part of the MOTIV (Modelling of Train Induced Vibration) project which is funded by the EPSRC under EP/K006002/1 and EP/K005847/1. All data published in this paper are openly available from the University of Southampton repository at http://dx.doi.org/10.5258/SOTON/D0077.

References

[1] D.J. Thompson: Railway Noise and Vibration: Mechanisms, Modelling and Means of Control. Elsevier, Oxford, UK (2008) (1st ed.).

[2] G. Lombaert, G. Degrande, S. Francois, D.J. Thompson, Ground-borne vibration due to railway traffic. *Proceedings of the 11th International Workshop on Railway Noise*, Uddevalla, Sweden, 9-13 September 2013, Notes on Numerical Fluid Mechanics & Multidisciplinary Design 126, 253-287.

[3] E. Kassa, J.C.O. Nielsen, Dynamic interaction between train and railway turnout: Full-scale field test and validation of simulation models. *Vehicle System Dynamics*, vol. 46 (SUPPL.1) (2008) 521-534.

[4] G. Kouroussis, D.P. Connolly, G. Alexandrou, K. Vogiatzis, Railway ground vibrations induced by wheel and rail singular defects. *Vehicle System Dynamics*, 53(10) (2015) 1500-1519.

[5] X. Sheng, C.J.C. Jones, M. Petyt, Ground vibration generated by a load moving along a railway track. *Journal of Sound and Vibration*, 228 (1) (1999) 129–156.

[6] G. Lombaert, G. Degrande, J. Kogut, S. François, The experimental validation of a numerical model for the prediction of railway induced vibrations. *Journal of Sound and Vibration*, 297(3-5) (2006) 512–535.

[7] M.F.M. Hussein, H.E.M. Hunt, A numerical model for calculating vibration from a railway tunnel embedded in a full-space. *Journal of Sound and Vibration*, 305 (2007) 401–431.

[8] J. O'Brien D.C. Rizos, A 3D FEM-BEM methodology for simulation of high speed train induced vibrations. *Soil Dynamics and Earthquake Engineering*, 25 (2005) 289–301.

[9] P.A. Costa, R. Calcada, A.S. Cardoso, Track–ground vibrations induced by railway traffic: In-situ measurements and validation of a 2.5D FEM-BEM model. *Soil Dynamics and Earthquake Engineering*, 32 (2012) 111-128.

[10] G. Kouroussis, D.P. Connolly, O. Verlinden, Railway-induced ground vibrations – a review of vehicle effects. *International Journal of Rail Transportation*, 2(2) (2014) 69-110..

[11] N. Triepaischajonsak, D.J. Thompson, A hybrid modelling approach for predicting ground vibration from trains. *Journal of Sound and Vibration*, 335 (2015) 147-173.

[12] J. Nielsen, E. Berggren, T. Lölgen, R. Müller, B.Stallaert, L. Pesqueux, Overview of methods for measurement of track irregularities important for ground-borne vibration. *RIVAS project*, SCP0-GA-2010-265754, Deliverable D2.5, Report to the EC (2012): http://www.rivas-project.eu/fileadmin/documents/RIVAS_CHALMERS_WP2_D2_5_FINAL.pdf

[13] E.G. Berggren, M.X.D. Li, J. Spännar, A new approach to the analysis and presentation of vertical track geometry quality and rail roughness. *Wear*, 265(9-10) (2008) 1488-1496.

[14] N. Triepaischajonsak, D.J.Thompson, C.J.C.Jones, J.Ryue, J.A.Priest, Ground vibration from trains: Experimental parameter characterization and validation of a numerical model. Proceedings of IMechE, Part F, *Journal of Rail and Rapid Transit* 225 (2011)140–153.

[15] V. K. Garg, R. V. Dukkipati, Dynamics of Railway Vehicle Systems. Academic Press, London, UK (1984).

[16] M.J.M.M. Steenbergen, A.V. Metrikine, The effect of the interface conditions on the dynamic response of a beam on a half-space to a moving load. *European Journal of Mechanics A/Solids*, 26 (2007) 33–54.

[17] S.L. Grassie, Rail irregularities, corrugation and acoustic roughness: characteristics, significance and effects of reprofiling. Proceedings of IMechE, Part F, *Journal of Rail and Rapid Transit* 226(5) (2012) 542-557.

[18] X. Sheng, C.J.C. Jones, D.J. Thompson, A theoretical model for ground vibration from trains generated by vertical track irregularities. *Journal of Sound and Vibration* 272 (3-55) (2004) 937-965.

[19] B. Faure, E. Bongini, Results of the parameter studies and prioritization for prototype construction for ballasted track. *RIVAS project*, SCP0-GA-2010-265754, Deliverable D3.2, Report to the EC (2012): http://www.rivas-project.eu/fileadmin/documents/RIVAS_WP3_Del_3.2.pdf

[20] A.A. Mirza, A. Frid, J.C.O. Nielsen, C.J.C. Jones. Ground vibrations induced by railway traffic - the influence of vehicle parameters. In: T. Maeda, P.E. Gautier, C. Hanson, B. Hemsworth, J.T. Nelson, B. Schulte-Werning, D.J. Thompson, P. de Vos (Eds.), *Noise and vibration mitigation for rail transportation systems. Proceedings of the Tenth International Workshop on Railway Noise, Nagahama, Japan, Notes on Numerical Fluid Mechanics and Multidisciplinary Design*, 118, Springer-Verlag, Berlin, 2012, pp. 259–266. (18–22 October 2010).